

Large-scale inhomogeneities of the intracluster medium: improving mass estimates using the observed azimuthal scatter

M. Roncarelli^{1,2}, S. Ettori^{2,3}, S. Borgani^{4,5,6}, K. Dolag^{7,8}, D. Fabjan^{5,6,9,10} and L. Moscardini^{1,2,3}

¹Università di Bologna, Dipartimento di Fisica e Astronomia, viale Berti Pichat 6/2, I-40127 Bologna, Italy

²Istituto Nazionale di Astrofisica (INAF) - Osservatorio Astronomico di Bologna, via Ranzani 1, I-40127 Bologna, Italy

³Istituto Nazionale di Fisica Nucleare (INFN) - Sezione di Bologna, viale Berti Pichat 6/2, I-40127 Bologna, Italy

⁴Università di Trieste, Dipartimento di Fisica, Sezione di Astronomia, via Tiepolo 11, I-34131 Trieste, Italy

⁵Istituto Nazionale di Astrofisica (INAF) - Osservatorio Astronomico di Trieste, via Tiepolo 11, I-34131 Trieste, Italy

⁶Istituto Nazionale di Fisica Nucleare (INFN) - Sezione di Trieste, Via Valerio 2, I-34127 Trieste, Italy

⁷Universitätssternwarte München, München, Germany

⁸Max-Planck-Institut für Astrophysik, Garching, Germany

⁹SPACE-SI, Slovenian Centre of Excellence for Space Sciences and Technologies, Aškerčeva 12, 1000 Ljubljana, Slovenia

¹⁰University of Ljubljana, Faculty of Mathematics and Physics, Jadranska 19, 1000 Ljubljana, Slovenia

27 March 2013

ABSTRACT

Achieving a robust determination of the gas density profile in cluster outskirts is a crucial point in order to measure their baryonic content and to use them as cosmological probes. The difficulty in obtaining this measurement lies not only in the low surface brightness of the ICM, but also in the inhomogeneities of the gas associated to clumps, asymmetries and accretion patterns. Using a set of hydrodynamical simulations of 62 galaxy clusters and groups we study this kind of inhomogeneities, focusing on the ones on the large scale that, unlike clumps, are the most difficult to identify. To this purpose we introduce the concept of *residual clumpiness*, $C_{\mathcal{R}}$, that quantifies the large-scale inhomogeneity of the ICM. After showing that this quantity can be robustly defined for relaxed systems, we characterize how it varies with radius, mass and dynamical state of the halo. Most importantly, we observe that it introduces an overestimate in the determination of the density profile from the X-ray emission, which translates into a systematic overestimate of 6 (12) per cent in the measurement of M_{gas} at R_{200} for our relaxed (perturbed) cluster sample. At the same time, the increase of $C_{\mathcal{R}}$ with radius introduces also a ~ 2 per cent systematic underestimate in the measurement of the hydrostatic-equilibrium mass (M_{he}), which adds to the previous one generating a systematic ~ 8.5 per cent overestimate in f_{gas} in our relaxed sample. Since the residual clumpiness of the ICM is not directly observable, we study its correlation with the azimuthal scatter in the X-ray surface brightness of the halo, a quantity that is well-constrained by current measurements, and in the y -parameter profiles that is at reach of the forthcoming SZ experiments. We find that their correlation is highly significant ($r_S = 0.6 - 0.7$), allowing to define the azimuthal scatter measured in the X-ray surface brightness profile and in the y -parameter as robust proxies of $C_{\mathcal{R}}$. After providing a function that connects the two quantities, we obtain that correcting the observed gas density profiles using the azimuthal scatter eliminates the bias in the measurement of M_{gas} for relaxed objects, which becomes 0 ± 2 per cent up to $2R_{200}$, and reduces it by a factor of 3 for perturbed ones. This method allows also to eliminate the systematics on the measurements of M_{he} and f_{gas} , although a significant halo to halo scatter remains.

Key words: Cosmology: large-scale structure of Universe – X-rays: galaxies: clusters – methods: N-body simulations.

1 INTRODUCTION

Clusters of galaxies are the most massive virialized systems of the Universe, they form in the knots of the cosmic web from which they continuously accrete material in the form of dark matter, gas and galaxies. Their importance for astrophysics is crucial, since they enclose information on the large-scale structure formation (see Kravtsov & Borgani 2012, for a review) and provide constraints on cosmological parameters which are independent with respect to cosmic microwave background (CMB), type-Ia supernovae and galaxy surveys (see, e.g., Allen et al. 2011, and references therein).

The precision with which clusters can be used as cosmological probes depends on the accuracy in the measurements of their mass, not only in terms of the total mass but also for its baryonic fraction $f_b \equiv M_b/M_{\text{tot}}$. If the value of f_b measured inside clusters matches the cosmic one (Ω_b/Ω_m) it can be used to obtain an independent estimate of Ω_m . However we know that the assumption of $f_b \simeq \Omega_b/\Omega_m$ holds only at large radii thus requiring the achievement of accurate observations also of cluster outskirts. In the recent years this point raised a great interest of the astrophysical community towards the study of clusters around and beyond the virial radius.

When moving outside the core the intracluster medium (ICM) is often affected by the presence of inhomogeneities and substructures, whose impact on the observed properties has been studied with a statistical approach (see, e.g., Jeltema et al. 2005; Böhringer et al. 2010; Andrade-Santos et al. 2012). The difficulty in observing cluster outskirts lies in the very low X-ray surface brightness of the ICM, that drops below the diffuse extragalactic X-ray background at $r \simeq R_{200}^1$ (see Roncarelli et al. 2006a,b). A possible method consists in stacking the images of different objects, as done by Eckert et al. (2012) who measured the density profiles and the azimuthal scatter in the X-ray surface brightness of 31 ROSAT-SPSC objects, showing a clear segregation between Cool-Core (CC) and No-Cool-Core (NCC) systems over the radial range 0.1–0.8 R_{200} , with the first ones exhibiting a scatter of 20–30 per cent, which corresponds to density variations of the order of 10 per cent. Above 0.8 R_{200} , the azimuthal scatter increases up to values of 60–80 per cent both in CC and NCC clusters, suggesting that they experience common physical conditions in shaping their X-ray surface brightness profiles. However the limit of the stacking technique is that it does not allow a precise determination of the temperature profiles of single objects. In this framework a great step forward has come from the *Suzaku* X-ray satellite that, thanks to its very low instrumental background, provided the first robust spectroscopical analyses of the regions close to R_{200} for the brightest objects (see, e.g., George et al. 2009; Bautz et al. 2009; Hoshino et al. 2010; Kawaharada et al. 2010; Simionescu et al. 2011; Humphrey et al. 2012; Sato et al. 2012). These works also highlighted the presence of a substantial azimuthal scatter, likely associated to clumps or inhomogeneities on the large scales, induced by major or even minor mergers that can cause sloshing and swirling motions in the ICM (see also Sanders & Fabian 2012; Churazov et al. 2012; Simionescu et al. 2012).

A promising complementary view with respect to X-rays can come from the observations of the thermal Sunyaev-Zeldovich effect (SZ, Sunyaev & Zeldovich 1970; Birkinshaw 1999; Rephaeli et al. 2005). The SZ signal is associated to temperature fluctuations in the CMB spectrum that are directly pro-

portional to the integral of the electron pressure along the line of sight. The SZ effect, in combination with the X-ray emission, can therefore probe the triaxial structure of the gas (De Filippis et al. 2005; Morandi et al. 2012; Sereno et al. 2012). Moreover, if the source is sufficiently extended to be resolved spatially even with the large beams available with present instruments such as *Planck* (as for nearby, hot systems like Coma, Planck Collaboration 2012) or multi-pixel bolometer arrays (as the *APEX-SZ* experiment, Basu et al. 2010, or *Bolocam* at the Caltech Submillimeter Observatory, Sayers et al. 2012) it can be used also to directly infer the pressure profile, under the assumption of the spherical symmetry of the ICM distribution, out to a significant fraction of the virial radius (see also Walker et al. 2012; Eckert et al. 2013).

From the theoretical point of view the modelisation of cluster outskirts is affected by different uncertainties with respect to cluster cores. On one side different feedback mechanisms do not affect significantly the behavior of temperature and density profiles, with gravity that constitutes the dominating physical process (Roncarelli et al. 2006b). On the other hand, the presence of shocks and turbulence may lead to the break of the hydrostatic equilibrium (see, e.g., Iapichino & Niemeyer 2008; Vazza et al. 2009; Burns et al. 2010; Nagai & Lau 2011, and references therein). In addition to that, hydrodynamical simulations showed how the outer ICM is affected by the presence of clumps (Roncarelli et al. 2006b; Nagai & Lau 2011) and inhomogeneities (Kawahara et al. 2008; Vazza et al. 2011) that may bias the reconstruction of the clusters' properties and explain the observed azimuthal scatter (see also Vazza et al. 2012; Zhuravleva et al. 2013). These large-scale inhomogeneities, both in gas densities and temperatures, are responsible for half of the ~ 30 per cent underestimate in the X-ray reconstructed hydrostatic mass, as highlighted by numerical simulations (see, e.g., Rasia et al. 2012; Piffaretti & Valdarnini 2008). The remaining part is mostly due to the residual bulk motions of the ICM, that preserve energy in non-thermalised form, not traceable with the measures of the density and temperature profiles alone (see, e.g., Rasia et al. 2006; Battaglia et al. 2012; Nelson et al. 2012, and references therein), but potentially detectable with spatially-resolved X-ray spectroscopy (see, e.g., the works on the Coma clusters by Schuecker et al. 2004 and Churazov et al. 2012).

In the work presented here we study the gas inhomogeneities present in the outskirts (close to R_{200} and beyond) of galaxy clusters and groups using a set of hydrodynamical simulations, with the objective of analyzing how the different physical processes may affect the degree of density fluctuations, together with the halo mass and its dynamical status. We concentrate our efforts in the definition of the density inhomogeneities associated to large-scale fluctuations, for which we introduce the concept of *residual clumpiness*, i. e. the clumpiness of the ICM after obvious clumpy structures have been removed. We discuss how this phenomenon may bias high the X-ray density profile measurements and explore, for the first time, the possibility of obtaining a direct measurement of this quantity via the analysis of the observed azimuthal scatter in the X-ray and y -parameter profiles of single objects. This method of estimating the residual clumpiness of the ICM allows us to propose a technique to reduce this bias and, therefore, to improve the precision of the measurement of the total mass and of the gas mass of galaxy clusters.

This paper is organized as follows. In the next Section we describe the set of hydrodynamical simulations used for our study. In Section 3 we characterize the gas inhomogeneities of our simulated haloes, we provide the definition of the residual clumpiness (C_R) and we study its dependence on cluster properties. Section 4

¹ In this work R_{200} is defined as the radius enclosing an average density equal to 200 times the critical density of the Universe $\rho_c \equiv \frac{3H_0^2}{8\pi G}$.

presents our results on the correlation between the azimuthal scatter and large-scale inhomogeneities of cluster outskirts. In Section 5 we quantify how the residual clumpiness biases the measurements of the gas mass, the hydrostatic-equilibrium mass and the gas fraction of the haloes and present a method to correct them using the observed azimuthal scatter. We summarize and draw our conclusions in Section 6.

2 THE SIMULATED CLUSTERS

The clusters object of our work belong to a set of 29 high-resolution re-simulations of galaxy cluster regions. A detailed description of the whole procedure to obtain them can be found in Bonafede et al. (2011). Here we provide a summary.

2.1 Simulation parameters

The cosmology assumed is a flat Λ CDM model with $\Omega_m = 0.24$ and $\Omega_\Lambda \equiv 1 - \Omega_m = 0.76$, a Hubble parameter $h = 0.72$ (being the Hubble constant $H_0 = 100 h \text{ km s}^{-1} \text{ Mpc}^{-1}$); we fix the primordial power spectrum of the DM fluctuations with slope $n = 0.96$ and normalization coherent with $\sigma_8 = 0.8$.

With these assumptions we carried out a large dark-matter (DM) only simulation using the GADGET-3 code, an evolved version of GADGET-2 (Springel 2005), with a periodic box of $1 h^{-1} \text{ Gpc}$ on a side and then identified the clusters in the $z = 0$ output with a *Friends of Friends* (FOF) algorithm, with linking length fixed to 0.17 times the mean inter-particle separation. The Lagrangian regions around $7R_{\text{vir}}$ from the centre of the 24 most massive objects (all with $M_{\text{vir}} > 10^{15} h^{-1} M_\odot$) were identified, traced back to their initial positions and then re-simulated at higher resolution using the zoomed initial conditions technique (Tormen et al. 1997). These re-simulations were run adding the hydrodynamical part by turning on the *Smoothed Particles Hydrodynamics* (SPH) code implemented in GADGET-2. This was done assuming $\Omega_b = 0.045$, with mass resolutions of $8.4 \times 10^8 h^{-1} M_\odot$ and $1.6 \times 10^8 h^{-1} M_\odot$ for the DM and gas particles, respectively, and with a Plummer-equivalent softening length for the gravitational force fixed to $\varepsilon = 5 h^{-1} \text{ kpc}$ in physical units at $z < 2$ and kept fixed in comoving units at earlier times.

In order to add statistics at the lower mass scales, another set of 5 galaxy clusters with masses $M_{200} = 1 - 5 \times 10^{14} h^{-1} M_\odot$ was selected at $z = 0$ and re-simulated with the same method, reaching a total of 29 re-simulated regions.

2.2 Feedback models

The set of 29 re-simulations was run with three different physical implementations. More detailed descriptions of these physical models can be found in Planelles et al. (2012).

(i) *NR*: non-radiative runs. They do not include any physical process except gravitation and hydrodynamics. Although unrealistic, they are useful as a test to check the impact of the various physical mechanisms.

(ii) *CSF*: runs including cooling, star formation, metal enrichment and galactic winds. The radiative cooling rates are computed following the procedure of Wiersma et al. (2009), considering also the contribution of metals in the hypothesis of a gas in (photo-)ionisation equilibrium by using the CLOUDY code (Ferland et al. 1998). Star formation is followed according to the multi-phase

model of Springel & Hernquist (2003) which also includes energy release by supernovae (SNe). Other feedback sources include heating from a spatially uniform, time dependent UV background (Haardt & Madau 1996) and metals released by type-II and type-Ia SNe and AGB stars according to the model of Tornatore et al. (2007). Finally, a kinetic feedback associated to galactic ejecta is implemented assuming a mass upload proportional to the star formation rate and a wind speed of $v_w = 500 \text{ km s}^{-1}$.

(iii) *AGN*: like *CSF*, but with wind speed reduced to $v_w = 350 \text{ km s}^{-1}$ and including also the feedback associated to gas accretion onto supermassive black holes (BHs). Its implementation is similar to the one of Springel (2005), with the inflow of matter that proceeds at Bondi rate up to the Eddington limit. In our implementation SPH particles stochastically selected for providing accretion into the BH feed it only with 1/4 of their mass at time, thus mimicking a more continuous flow of material. The amount of kinetic energy released by each BH particle is given by

$$\dot{E}_{\text{feed}} = \epsilon_r \epsilon_f \dot{M}_{\text{BH}}^2, \quad (1)$$

being ϵ_r and ϵ_f the radiative efficiency and the fraction of energy coupled to the gas, respectively. In our implementation these two free parameters were fixed at $\epsilon_r = 0.1$ and $\epsilon_f = 0.05$, increasing to $\epsilon_f = 0.2$ when the accretion rate is smaller than one-hundredth of the Eddington limit (see also Sijacki et al. 2007; Fabjan et al. 2010). We will take this model as our reference one.

2.3 Definition of the halo sample

Since the volume of each of the 29 re-simulations encloses a spherical region of radius much larger than the virial radius of the main object, it is common to find other haloes included in the final $z = 0$ outputs. Hence, in order to increase the statistical significance of our results and to characterize better also the low mass objects, we included in our sample all the ‘secondary’ haloes with $M_{200} > 10^{14} h^{-1} M_\odot$ in at least one of the three runs. The values of M_{200} were computed starting from the FOF catalogues and applying a *Spherical Overdensity* algorithm. This increases our halo sample to a total of 62 objects in different mass ranges. A histogram of their masses is shown in Fig. 1.

In order to study the dependence of the clumpiness on the mass of the halo and on its dynamical properties, we divide our objects into subsamples: given the amplitude of our initial sample, this can be done without losing statistical robustness. In particular we will adopt the following two definitions:

- *clusters/groups* (28 and 34 objects, respectively), according to their M_{200} being higher/lower than $5 \times 10^{14} h^{-1} M_\odot$,
- *relaxed/perturbed* (30 and 32 objects, respectively), according to a definition based on the clumpiness and described in Section 3.3.

The histogram of Fig. 1 shows also these classifications. It is worth to mention that clusters tend to be slightly more perturbed (16 and 12 relaxed) than groups (16 and 18) due to their more active dynamical state.

3 DENSITY INHOMOGENEITIES

3.1 The gas clumpiness

A commonly used indicator of the degree of inhomogeneity of a medium is its clumpiness. Even if it is normally used to measure

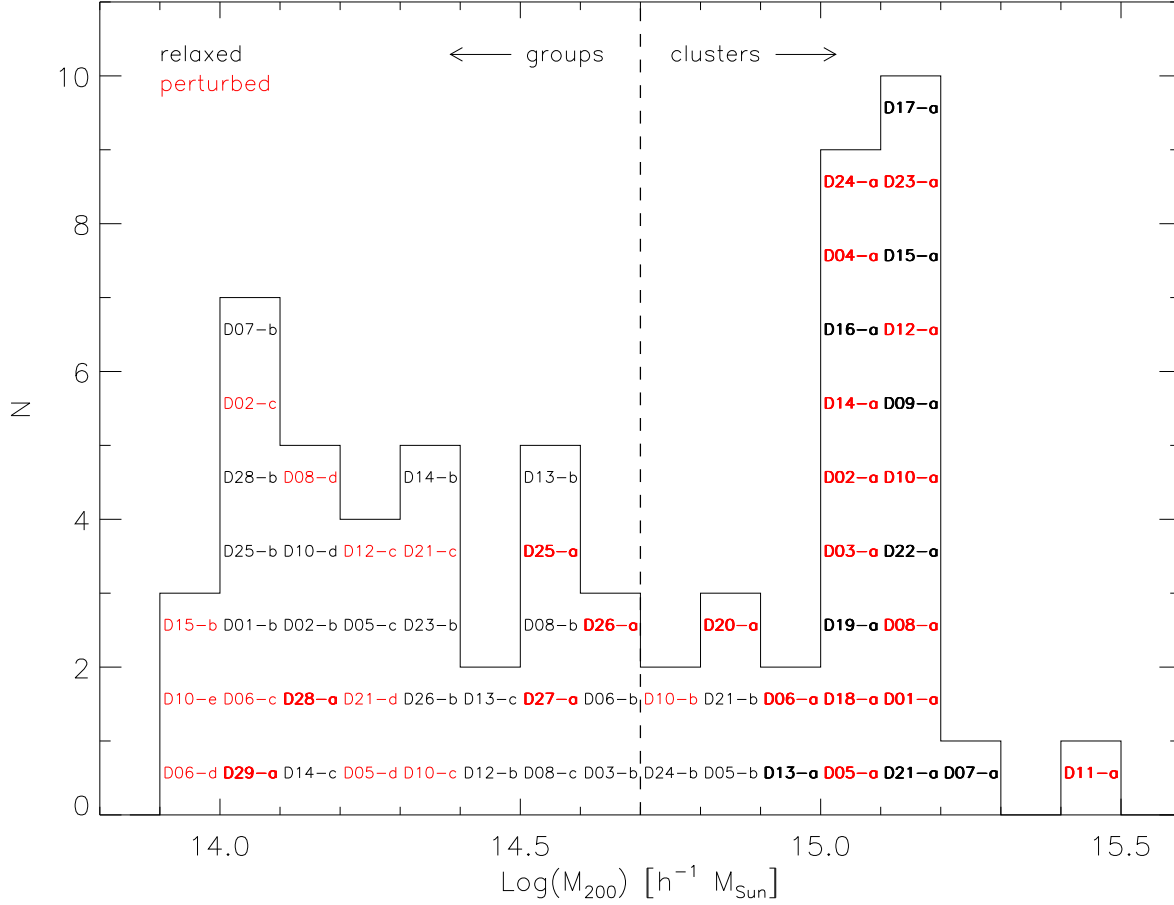


Figure 1. Distribution of M_{200} for the sample of 62 simulated haloes in our reference (AGN) run. Cluster names correspond to the ones given in Bonafede et al. (2011), with the addition of D25–D29 that indicate the low mass objects re-simulations. The main haloes of each re-simulation are dubbed $DXX-a$ (bold face) while their satellites are indicated with letters from $-b$ to $-e$ in decreasing mass order. The vertical dashed line indicates the mass limit of $5 \times 10^{14} h^{-1} M_{\odot}$ used to separate groups (34 objects) and clusters (28). Objects marked in red correspond to perturbed (32) haloes, while black indicates relaxed (30) ones, as defined in Section 3.3.

the amount of small clumps in an approximately uniform medium, its general definition allows us to use it also to quantify the amount of inhomogeneity associated to large-scale density fluctuations.

The clumpiness or clumping factor C of a fluid element is defined by the following formula:

$$C \equiv \frac{\langle \rho^2 \rangle_V}{\langle \rho \rangle_V^2}, \quad (2)$$

where ρ is the fluid density and the brackets $\langle \rangle_V$ indicate the average calculated over its volume. The clumpiness is therefore defined as being equal to unity for a perfectly uniform medium and > 1 otherwise, with higher values indicating higher levels of inhomogeneities. When writing explicitly the integrals, eq. (2) can be expressed as

$$C = \frac{V}{M^2} \int_V \rho^2 dV, \quad (3)$$

where M and V are the mass and volume of the gas element, respectively. Since we are using SPH simulations, for a given distance r from the cluster centre, we compute $C(r)$ by converting eq. (3) into

$$C(r) = \frac{\sum_i m_i \rho_i}{(\sum_i m_i)^2} V_{\text{shell}}, \quad (4)$$

where the sum \sum_i is computed over the particles with distance

between r and $r + dr$, m_i and ρ_i are the mass and density, respectively, of the i -th SPH particle and $V_{\text{shell}} = \frac{4}{3}\pi[(r + dr)^3 - r^3]$ is the volume of the shell used to compute the quantity.

For the purpose of our work, for every halo we compute the clumpiness and the other physical quantities in the range $0 < r < 2R_{200}$, in 50 equally spaced bins.

3.2 Separating small clumps from large-scale inhomogeneities: the residual clumpiness

The amount of clumpiness of the ICM is caused by two different phenomena: the presence of small dense clumps and the density fluctuations on larger scales associated to asymmetries in the large-scale accretion pattern, with the first one that constitutes the dominating contribution. Here we describe a method that proves useful to isolate these two components in order to treat them separately. This aspect is particularly important when we consider that the physical properties of clumps and their abundance depend on the processes of cooling and star formation and, consequently, their presence in our simulated clusters is subject to the uncertainties associated to the implementation of physical models in hydrodynamical codes. Moreover, several works (see, e.g., Mitchell et al. 2009; Sijacki et al. 2012, and references therein) highlighted how SPH simulations produce a higher quantity of dense clumps with

respect to Eulerian ones. This is associated to the different numerical viscosity, intrinsic in the codes themselves, that causes a lower dissipation efficiency in SPH simulations.

To this purpose, we follow the volume-selection scheme described in Roncarelli et al. (2006b) to compute the profiles of galaxy clusters close to and beyond R_{200} . This method consists in sorting the SPH particles belonging to a given radial bin according to their physical density. Then, starting from the most diffuse one, we sum up their volumes (defined as $V_i = m_i/\rho_i$) until we reach a fixed fraction, 99 per cent in our case, of the total volume of the radial bin and consider only these particles to compute C : the remaining particles are identified as clumps and considered separately in our computation. This procedure proved to be effective in excising all the dense and cold clumps that are highly dependent on the physical assumptions, as well as the small X-ray bright regions that are usually masked out in observational analyses, thus providing a good description of the global properties of the ICM such as density, temperature and X-ray surface brightness (see the discussion in Roncarelli et al. 2006b). Recently, a similar approach has also been applied to Eulerian simulations by Zhuravleva et al. (2013) who approximate the density distribution of the gas in different radial bins with a lognormal distribution and mark as clumps the cells with density above values fixed in terms of the σ of the distribution (see also Khedekar et al. 2012). In fact, although applied in completely different numerical simulations (grid-based and SPH), the two methods are formally identical, with their threshold of $f_{cut} = 3.5$ that matches our 99 per cent criterion. For what concerns the possible biases caused by unresolved clumpy gas, we have verified that they have a small impact on our results. For more details about this point and about the clumps physical properties, we refer to the Appendix A. We use this method to define the *residual clumpiness* associated to large-scale perturbations, $C_{\mathcal{R}}$, and to separate it from the total one: this allows us to note that the value of $C_{\mathcal{R}}$ is about one order of magnitude lower with respect to C inside R_{200} (see the discussion in Section 3.3).

We have also checked that in most of the cases lowering the threshold value to 95 per cent (i.e. increasing by a factor of 5 the volume of gas considered as small-scale clumps) produces negligible changes in $C_{\mathcal{R}}$. However, when the cluster is perturbed by the presence of a large halo (e.g. an infalling group), lowering the density threshold for the clumps identification can change the final result by up to 50 per cent in the radial bins corresponding to the halo distance. A sketch of the application of this method is shown in Fig. 2 for two different cases. These X-ray surface brightness maps show that when cutting the 1 per cent densest volume (from top to middle panels) we are able to remove all obvious clumpy structures that are associated to the brightest peaks. When cutting the 5 per cent of the volume (bottom panels) the surface brightness remains almost unchanged for a relaxed halo (left) while for a dynamically perturbed one (right) the infalling halo on the bottom right is progressively removed, indicating that it is difficult to define a precise threshold to separate the two components. The effect on the definition of $C_{\mathcal{R}}$ can be clearly seen in the plot of Fig. 3, where we show the residual clumpiness as a function of radius computed for these two haloes by adopting the two different volume threshold: while for D17-a the value of $C_{\mathcal{R}}$ is almost independent on the threshold chosen up to R_{200} , for D12-a the presence of the infalling halo at $r \simeq 0.5R_{200}$ produces a difference of about 0.25.

For this reason we use the difference between the value of $C_{\mathcal{R}}$ computed with these two limits to introduce another useful halo classification. We sort our haloes according to the maximum relative difference between $C_{\mathcal{R}}^{99}(r)$ and $C_{\mathcal{R}}^{95}(r)$ for $r < R_{200}$ and split

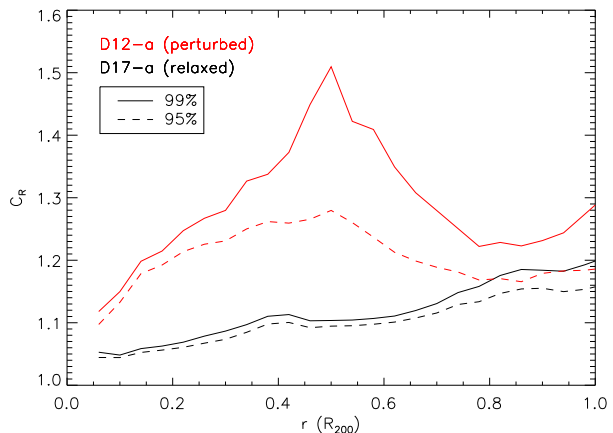


Figure 3. Residual clumpiness as a function of distance from the centre computed for the two haloes shown in the maps of Fig. 2: D17-a (black lines, lower values) and D12-a (red lines, higher values). The value of $C_{\mathcal{R}}$ has been computed adopting two different thresholds for the volume-clipping method: 99 per cent (solid lines) and 95 per cent (dashed lines). The physical model assumed is the reference one (AGN).

our 62 haloes roughly into two equal subsamples: we define a halo as *relaxed* when this difference is less than 8 per cent, and *perturbed* otherwise. In this way, we end up with 32 perturbed haloes and 30 relaxed ones. For this last set we can consider our value of $C_{\mathcal{R}}$ to represent a robust estimate of the amount of inhomogeneities associated to large-scale asymmetries. We also verified that our classification has a good correspondence with an observational-like classification based on X-ray images. We refer the reader to Appendix B for the details on this point.

3.3 Dependence on physics and environment

We show on the top panel of Fig. 4 the results of the clumpiness as a function of radius for our whole sample of objects, computed considering the three physical implementations described in Section 2.2. When radiative cooling is included (*CSF* and *AGN* models) the level of clumpiness is very high and ranges from ~ 3 close to the centre up to ~ 10 close to R_{200} . When extending to outer regions the value of C increases exponentially reaching values of the order of 100 at $2R_{200}$, with no significant difference when including BH feedback. When neglecting gas cooling (*NR*), the values drop down by a factor of 5–10 over the whole range, indicating that the value of C is mainly associated to small cold clumps.

However, when comparing our results with observational estimates one must consider that the cold dense gas at $T < 10^5$ K does not produce any observable clumpiness in X-ray images. This makes the plotted *NR* profile model a reference for the observed value of C without considering any detection of emitting clumps. For this reason we conclude that the value of ~ 16 obtained by Simionescu et al. (2011) for the Perseus cluster is not realistic, since it is sufficient to exclude cold gas from our simulations to obtain significantly lower values.

The lower panel of Fig. 4 shows the values of $C_{\mathcal{R}}$, which corresponds to the value of the clumpiness computed after applying the 1 per cent volume-clipping described in Section 3.2. With this method the difference associated to the physical implementations disappears almost completely, even for the *NR* model: this indicates that large-scale inhomogeneities do not depend on the phys-

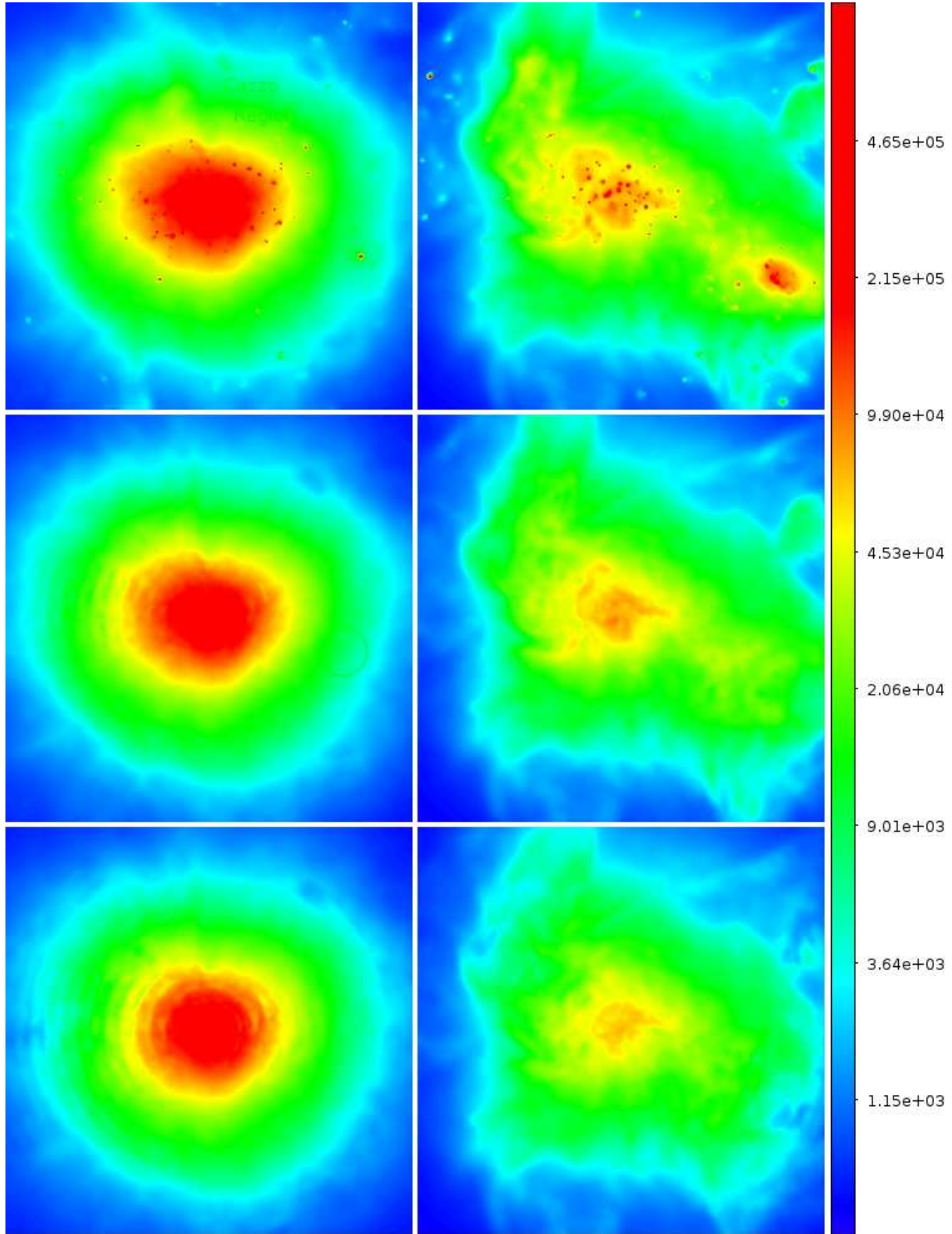


Figure 2. Bolometric (0.1–10 keV) X-ray flux (in units of $\text{counts s}^{-1} \text{cm}^{-2}$) of a relaxed cluster (D17-a, left column) and a perturbed one (D12-a, right column). The size of each map is $1R_{200}$ per side. In the first row all the particles have been considered, in the second and third ones the volume cut has been applied considering the 99 per cent and 95 per cent threshold, respectively.

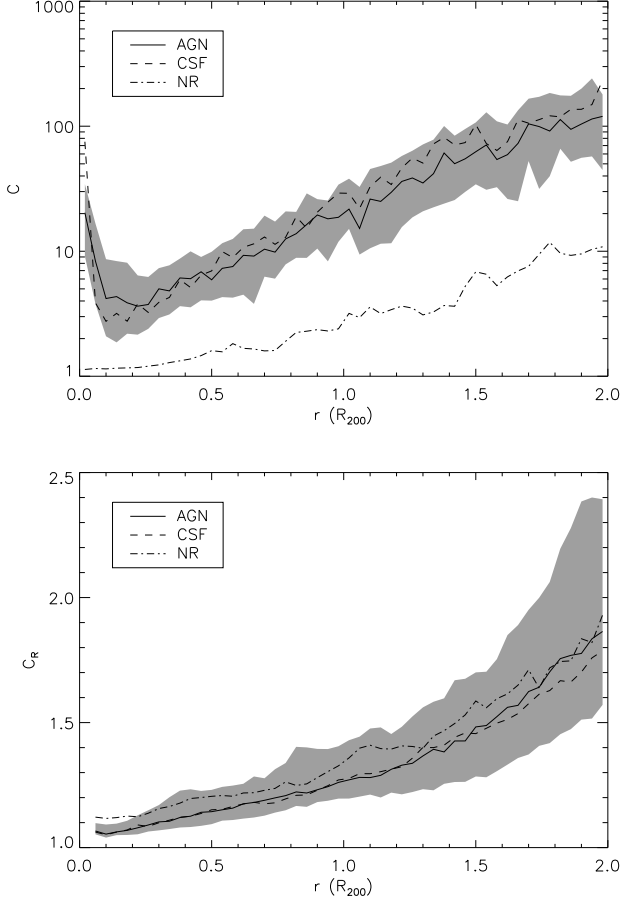


Figure 4. Upper panel: gas clumpiness of our simulated haloes as a function of distance from the centre, for the *AGN* (solid line), *CSF* (dashed) and the *NR* model (dot-dashed). The values represent the median of 62 objects, the grey-shaded region encloses the quartiles of the *AGN* model (the quartile regions of the other two runs have similar sizes). Lower panel: same as upper panel but for the residual clumpiness, i.e. after applying our volume-clipping method.

ical process that occur in the ICM, but on the intrinsic dynamical properties of the halo itself. In this case the median of C_R computed on the whole sample has a value very close to 1 (e.g. almost uniform medium) close to the centre and grows constantly up to 1.3–1.4 at R_{200} . There is a significant variance between the different haloes with about 25 per cent of objects having values of ~ 1.4 . Outside R_{200} the value of C_R reaches ~ 2 at $2R_{200}$, together with an increase of the dispersion between the objects: this reflects the intrinsic difference between the environment of the clusters’ and groups’ outskirts that can contain or not infalling haloes and accreting filaments.

This independence with respect to the physical implementation is partially in contrast with what obtained by Zhuravleva et al. (2013) that observe a slightly higher degree of inhomogeneity of the bulk in their NR runs, of the order of $\Delta C = 0.1 - 0.2$. In fact, also in our simulations we see a small ($\Delta C \sim 0.04$) systematic excess in our NR model, associated to the hot-dense tail of the ICM distribution. This discrepancy probably indicates a different cooling efficiency in the simulations analysed here and by Zhuravleva et al. (2013).

It is interesting to see how the trend of C_R varies when con-

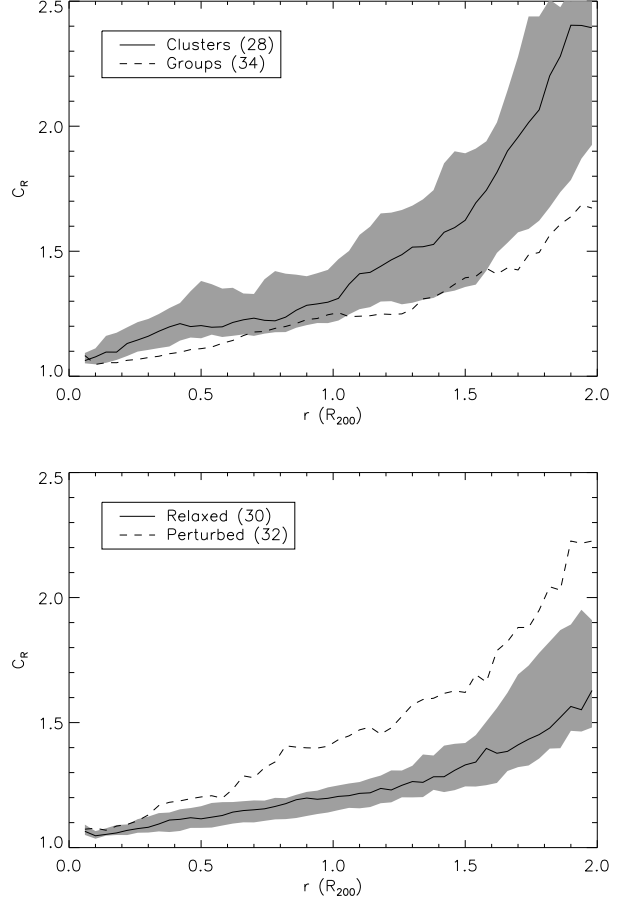


Figure 5. Upper panel: residual gas clumpiness, i.e. after applying the volume-clipping method, for clusters (solid line) and groups (dashed line) as a function of distance from the centre for our reference model. The values represent the median of the sample (28 and 34 objects, respectively), and the grey-shaded region encloses the quartiles of the clusters sample. Lower panel: same as upper panel but with relaxed (30 objects, solid line) and perturbed (32 objects, dashed line) haloes.

sidering the mass of the halo and its dynamic status. We show in the top panel of Fig. 5 the results of C_R computed when separating the haloes according to their mass into groups and clusters (see Section 2.3). Clusters have on average a higher value of C_R of the order of ~ 0.1 , with larger differences outside R_{200} : this is due to the fact that massive objects have higher probability of accreting material even at later epochs, while galaxy groups are dynamically older, more dynamically stable and, therefore, more uniform. When separating relaxed and perturbed objects according to our definition (see Section 3.2) the difference is even more remarkable, as it can be seen in the bottom panel of Fig. 5. While close to the centre the two samples have very similar values of C_R , the presence of accreting structures pushes the residual clumpiness of perturbed objects beyond 1.5 at R_{200} . On the other side, relaxed haloes show all the same trend with C_R raising linearly to 1.3–1.5 at R_{200} : the residual clumpiness of these objects should be considered as an indicator of the amount of inhomogeneities common to all haloes, even the more dynamically stable, and connected to their departure from spherical symmetry and to the density fluctuations associated to the large-scale accretion patterns.

We observe as well that the differences in C_R associated to

the clusters/groups classification can be explained completely by the different correlation with the relaxed/perturbed one, (i. e. clusters have higher values of $C_{\mathcal{R}}$ because they are on average more perturbed than groups), making the latter classification the more interesting for our purposes. We note also that the trends that we observe are similar to those found by Zhuravleva et al. (2013), (we refer to their 'bulk CSF' results), both in terms of radial dependence and with respect to the dynamical state of the haloes.

4 THE AZIMUTHAL SCATTER AS A DIAGNOSTIC OF THE RESIDUAL CLUMPINESS

4.1 The azimuthal scatter

As said, the clumpiness of the ICM is not a directly measurable quantity. Here we investigate the possibility of obtaining an estimate from the observed azimuthal scatter of the X-ray and SZ profiles of the haloes.

Following Vazza et al. (2011), we define the azimuthal scatter of an observable quantity x as

$$\sigma_x(r) \equiv \sqrt{\frac{1}{N} \sum_{i=1}^N \left(\frac{x_i(r) - \bar{x}(r)}{\bar{x}(r)} \right)^2}, \quad (5)$$

where N is the number of azimuthal sectors, $x_i(r)$ is the radial profile of the quantity in a given sector and $\bar{x}(r)$ is the average over the N sectors at distance r from the centre. In our case we fix $N = 12$, so that each sector corresponds to 30 degrees: this value is enough to account for all of the main azimuthal fluctuations associated to typical ICM inhomogeneities (see the discussion in Vazza et al. 2011). For the purpose of our work we consider the scatter in the X-ray surface brightness (computed in different bands) and in the thermal SZ effect.

We compute the X-ray surface brightness for every halo in the same 50 radial bins and in the 12 different sectors by assuming an APEC emission model (Smith et al. 2001), by fixing the redshift² of our clusters to $z = 0$. Since our AGN model follows also the enrichment of metals with the recipe of Tornatore et al. (2007), we consider also the contribution from different chemical species in the computation of the emissivity of the SPH particles (the details of the procedure are described in Roncarelli et al. 2012). For what concerns the SZ scatter, the method to compute the value of the y -parameter from our SPH simulation is the same as in Roncarelli et al. (2007). For these computations we are considering all the SPH particles, without applying the volume-clipping method (see Section 3.2).

We show in the upper panel of Fig. 6 the azimuthal scatter as a function of distance from the centre for the value of the y -parameter and the surface brightness in three different X-ray bands. At each distance we show the median computed over the whole sample of 62 haloes in the AGN model. The general observed trend is an increase of the azimuthal scatter with radius, with the value of σ_y going from ~ 0 at the centre to ~ 0.3 at R_{200} . The scatter associated to the X-ray surface brightness is 2–3 times higher at all distances, with lower energy bands (0.3–0.8 and 0.5–2 keV) having higher values with respect to the hard 2–10 keV band, indicating that these inhomogeneities are associated to gas at temperatures

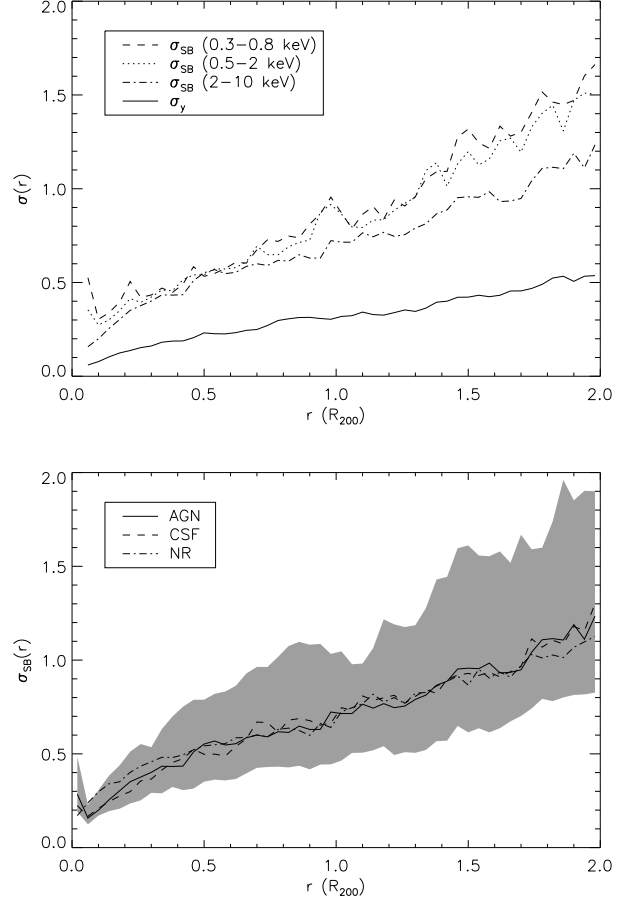


Figure 6. Upper panel: azimuthal scatter of the y -parameter (solid line) and of the X-ray surface brightness in the 0.3–0.8, 0.5–2 and 2–10 keV bands (dashed, dotted and dot-dashed line, respectively) as a function of distance from the cluster centre. The values represent the median computed over the whole sample of 62 haloes in 12 azimuthal sectors. Lower panel: same as upper panel but for the 2–10 keV surface brightness only, computed with three different physical implementations: AGN (solid line), CSF (dashed) and NR (dot-dashed). The grey-shaded area encloses the quartiles of the clusters sample for our reference model.

around 0.5–1 keV, that has the peak of its emission at soft X-ray energies.

It is interesting to note that when studying how the azimuthal scatter varies with respect to the assumed physics and to the halo classifications, the trend is very similar with respect to $C_{\mathcal{R}}$, rather than the global clumping factor C (refer to Section 3.3). For instance, the lower panel of Fig. 6 shows that the value of σ_{SB} is almost independent of the assumed physical model. When looking at the dependence on the mass and the dynamical status of the halo (upper and lower panels of Fig. 7, respectively) we can see that on average galaxy clusters show a slightly higher azimuthal scatter, while perturbed systems have values of σ which are higher by a factor of 2 with respect to relaxed ones at R_{200} .

4.2 Correlating the clumpiness with the azimuthal scatter

Since we have shown that clumpiness and azimuthal scatter have similar radial trends, here we address directly the question whether

² Since we are interested in the azimuthal scatter of the X-ray surface brightness and not in its absolute value, fixing the redshift has effect only in the definition of the X-ray bands.

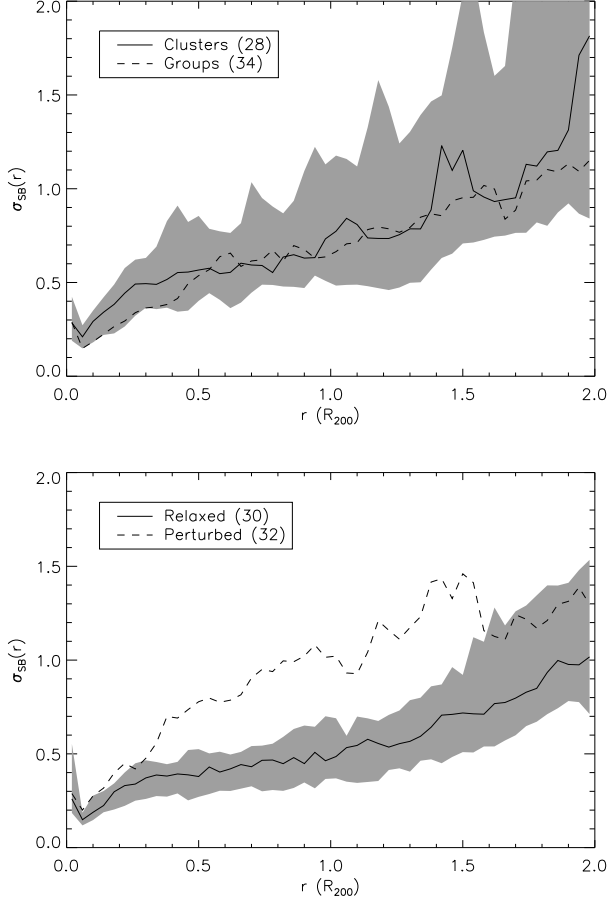


Figure 7. Upper panel: azimuthal scatter of the 2–10 keV surface brightness for clusters (solid line) and groups (dashed) as a function of projected distance from the centre for our reference model. The values represent the median of the two samples (28 and 34 objects, respectively), and the grey-shaded region encloses the quartiles of the clusters sample. Lower panel: same as upper panel but with relaxed (30 objects, solid line) and perturbed (32 objects, dashed line) haloes.

a tight correlation exists between these variables and if there exists a possible relation that can connect one with the other.

To this purpose we perform a statistical analysis of these variables by computing the Spearman’s rank correlation, r_S , of C and of $C_{\mathcal{R}}$ with the scatter in the X-ray and SZ profiles of our clusters. We restrict our analysis to the interval $0.15 < r/R_{200} < 1.5$, in order to cut out the core, and to the sample of the relaxed haloes for which the definition of $C_{\mathcal{R}}$ is more robust. Given the large sample of haloes available, these restrictions do not affect the robustness of our computation. The results are shown in Table 1.

The main conclusion that can be drawn from these values is that the azimuthal scatter of both X-ray and SZ profiles has a very high degree of correlation with the values of $C_{\mathcal{R}}$, i. e. with the inhomogeneities on the large scales: in fact, the values of $r_S = 0.6–0.7$ indicate that it is possible to describe $C_{\mathcal{R}}$ as a monotonic increasing function of σ_y and σ_{SB} . On the other side when considering the correlation of the different azimuthal scatters with the total clumpiness, C , the correlation still exists although being much weaker. It is worth to point out also how the trend with the X-ray energy is opposite in the two cases. Since clumps embed lower temperature ICM, softer bands are more correlated to C with respect to the hard

Table 1. Spearman’s rank correlation (r_S) of the values of C and $C_{\mathcal{R}}$ (second and third column, respectively) with the azimuthal scatter in the X-ray surface brightness in different bands (second to fourth row, respectively) and in the y -parameter profiles (fifth row). The values analysed are taken from the 30 relaxed haloes considering the bins in the range $0.15 < r/R_{200} < 1.5$.

	C	$C_{\mathcal{R}}$
σ_{SB} (0.3–0.8 keV)	0.32	0.59
σ_{SB} (0.5–2 keV)	0.30	0.60
σ_{SB} (2–10 keV)	0.23	0.61
σ_y	0.35	0.68

one. On the other side, when clumps are excised, the densest gas is also hotter thus the correlation $C_{\mathcal{R}}-\sigma_{SB}$ increases at higher energy.

More in the detail, we show in Fig. 8 the correlation between $C_{\mathcal{R}}$ and the scatter in the 2–10 keV band (top panel): although there is a significant dispersion, the trend of increasing clumpiness with increasing value of σ_{SB} is clear. The same applies also when considering the scatter in the y -parameter (bottom panel). When analysing the dispersion of the relation, it is clear also the trend of higher values of $C_{\mathcal{R}}$ for increasing radii (indicated by the different colors), as already discussed for Figs. 4 and 5.

Since it is not possible to define *a priori* the relation between scatter and clumpiness, we proceed empirically by introducing the following function

$$C_{\mathcal{R}}^{\text{est}}(\sigma, r) = 1 + \frac{\sigma}{\sigma_0} + \frac{r}{r_0} \quad (6)$$

that connects the azimuthal scatter σ and the distance from the center r with an estimate of the clumpiness $C_{\mathcal{R}}^{\text{est}}$. The choice of this expression is made in order to have a simple increasing function of both σ and r (which holds for $\sigma_0 > 0$ and $r_0 > 0$), and $C_{\mathcal{R}}^{\text{est}}(\sigma = 0, r = 0) = 1$.

Given the two free parameters, σ_0 and r_0 , for every observable quantity object of our analysis (i.e. azimuthal scatter in the X-ray surface brightness and in the y -parameter) we determine their best-fit values by fitting³ the expression of eq. (6) using the points displayed in Fig. 8, i.e. $C_{\mathcal{R}}$ as a function of σ and r . Again, we restrict this calculation to the 30 relaxed clusters and to the range $0.15 < r/R_{200} < 1.5$. The results are shown in Fig. 8, together with the residuals, for the 2–10 keV band and for the y -parameter. It is clear that the best-fit function provides a good global description of the relation $C_{\mathcal{R}}-(\sigma, r)$, with almost all of the points that have an estimate within 10 per cent of the true value. Furthermore, we note how the diagonal dashed line corresponding to best-fit relation in the limit of $r = 0$ defines well the “forbidden” region of the $C_{\mathcal{R}}-\sigma$ plane, below the line itself. Table 2 shows the best-fit values for all the three X-ray bands and for the thermal SZ effect.

5 IMPROVING MASS ESTIMATES

We have shown in the previous section that it is possible to obtain an estimate of the large-scale inhomogeneities ($C_{\mathcal{R}}$) from the azimuthal scatter in the X-ray surface brightness and y -parameter.

³ In the fitting procedure we omit to assign errors to our data.

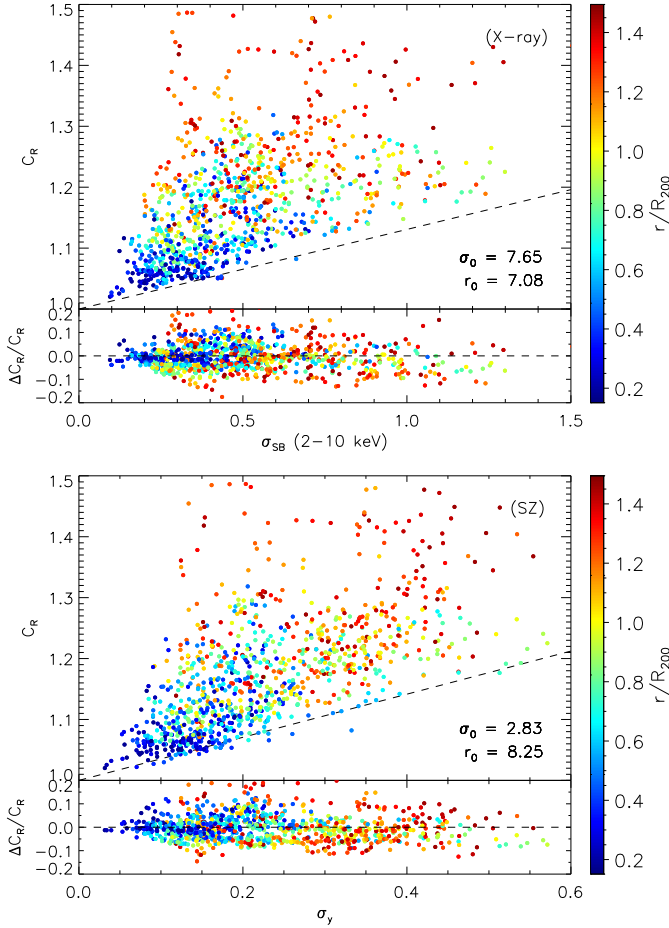


Figure 8. Upper panel: correlation between the azimuthal scatter in the 2–10 keV band and $C_{\mathcal{R}}$. The points considered correspond to the sample of the 30 relaxed haloes in the range $0.15 < r/R_{200} < 1.5$ (a total of 990 points, 33 for each halo) and their colors indicate the radial distance, increasing from blue to red. The quantities indicated (σ_0 and r_0 in units of R_{200}) are the best-fit values obtained using the formula of eq. (6) and the lower part shows the residuals with respect to the model in terms of relative difference in the clumpiness value. The diagonal dashed line indicates the relation $C_{\mathcal{R}} = 1 + \sigma/\sigma_0$, i.e. the best-fit formula in the limit of $r = 0$. Bottom panel: same as upper panel but for the scatter in the y -parameter.

The question that arises is whether it is possible to use the observed value of $\sigma(r)$ as a function of the distance from the cluster centre, to improve the estimates of the gas density profile and, consequently, the measurement of M_{gas} and M_{he} .

5.1 Correcting the gas density profile

The estimate of the gas density profile $\rho(r)$ from the X-ray surface brightness is affected by the problem that the corresponding emissivity $\epsilon_X(r)$ in a fixed band depends on the squared gas density: $\epsilon_X \propto \rho^2$. Given the definition of eq. (2), an observer that ignores the residual clumpiness of the gas and assumes spherical symmetry obtains

$$\rho_X(r) = \sqrt{C_{\mathcal{R}}(r)} \rho(r), \quad (7)$$

which corresponds to a systematic overestimate.

If we consider the observed azimuthal scatter profile, $\sigma(r)$,

and use the relation of eq. (6) to obtain an estimate of $C_{\mathcal{R}}$, we can correct our measurement of the density profile as follows

$$\hat{\rho}(r) = \frac{\rho_X(r)}{\sqrt{C_{\mathcal{R}}^{\text{est}}(\sigma, r)}}. \quad (8)$$

As examples, we show in Fig. 9 the application of this method to the two clusters of Fig. 2. The relaxed D17-*a* cluster (left panel) shows reconstructed density profiles very close to the true value⁴, with differences smaller than 2 per cent up to R_{200} . On the other side, the corresponding uncorrected X-ray profile overestimates the true value by 5–10 per cent over the whole $r > 0.4R_{200}$ range.

When looking at the D12-*a* cluster (right panel), the presence of the disturbing structure still produces an overestimate of the corrected density profiles of about 5–10 per cent in correspondence of the clumpiness peak. However, even in this case the improvement with respect to the original ρ_X profile overestimate is remarkable, through all the radial range.

This method can be directly applied to the observed density profiles and scatter of Eckert et al. (2012). In fact, they obtained a measurement of σ_{SB} in the soft 0.5–2 keV band in their 31 ROSAT-PSPC objects (we refer to their Fig. 7, entire sample) up to R_{200} . By using this quantity to estimate the residual clumpiness, we obtain an approximate value of $C_{\mathcal{R}}^{\text{est}} = 1.2$ at $r \sim R_{200}$, that corresponds to an overestimate of ~ 8 per cent in the gas density. This consideration leads to mitigate the existing conflict between their observed density profiles and the simulated ones, although not enough to solve the problem completely.

5.2 Correcting the gas mass bias

If its gas density profile $\rho(r)$ is known, then the gas mass of the halo enclosed by R_{200} can be obtained from the following formula:

$$M_{\text{gas}} = 4\pi \int_0^{R_{200}} \rho(r) r^2 dr. \quad (9)$$

However, the density bias described by eq. (7) reflects also into the gas mass estimate,

$$M_{\text{gas},X} = 4\pi \int_0^{R_{200}} \sqrt{C_{\mathcal{R}}(r)} \rho(r) r^2 dr, \quad (10)$$

that leads to a bias in the gas mass measurement

$$b(M_{\text{gas}}) \equiv \frac{M_{\text{gas},X} - M_{\text{gas}}}{M_{\text{gas}}} \quad (11)$$

which is always > 0 reaching null value only in the limit of a perfectly uniform medium ($C_{\mathcal{R}} = 1$).

Given our set of simulated clusters and groups, we can obtain the expected value of $b(M_{\text{gas}})$ from their density and clumpiness profiles. The results are shown in the top panel of Fig. 10: typical values correspond to overestimates of 5–10 per cent, with the more perturbed haloes that can reach overestimates around 20–30 per cent.

If we substitute in eq. (9) the corrected density profile of

⁴ Here we are considering the density profiles after applying the volume-clipping method described in Section 3.2, so we are implicitly assuming that small clumps have been efficiently removed in X-ray observations.

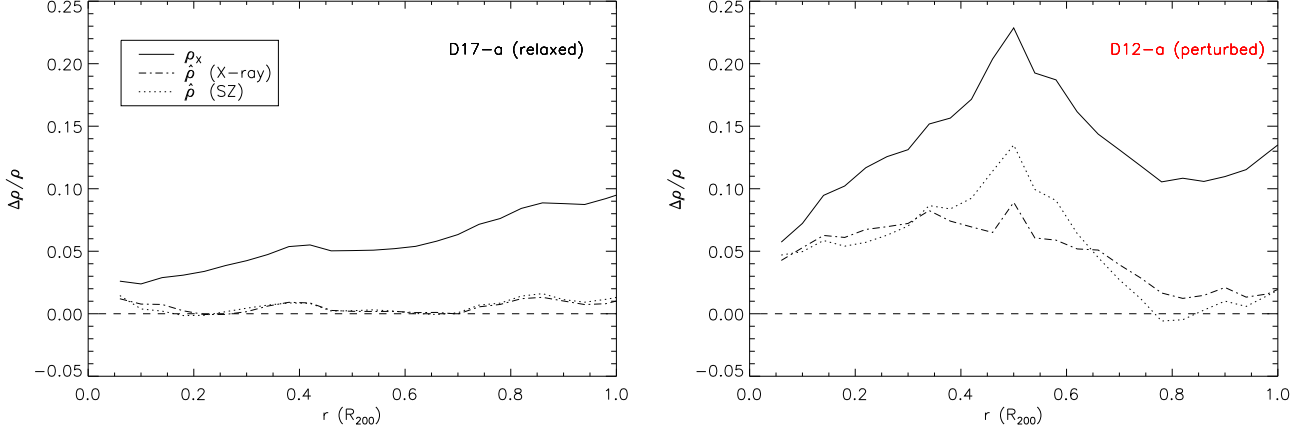


Figure 9. Sketch of the gas density correction method applied to the two clusters shown in the maps of Fig. 2: D17-*a* (left panel) and D12-*a* (right panel). We show the radial dependence of the relative differences between the true gas density and the uncorrected measured density (solid line), the density after applying the X-ray and SZ corrections (dot-dashed and dotted line, respectively). The horizontal dashed line shows the ideal case of perfect density profile reconstruction ($\Delta\rho = 0$).

eq. (8), we obtain a new estimate of the gas mass

$$\begin{aligned}\widehat{M}_{\text{gas}} &= 4\pi \int_0^{R_{200}} \hat{\rho}(r) r^2 dr = \\ &= 4\pi \int_0^{R_{200}} \sqrt{\frac{C_{\mathcal{R}}(r)}{C_{\mathcal{R}}^{\text{est}}(\sigma, r)}} \rho(r) r^2 dr\end{aligned}\quad (12)$$

which provides a good approximation of M_{gas} as much as $C_{\mathcal{R}}^{\text{est}}$ is an accurate estimate of the residual clumpiness.

We verify the accuracy of this method by applying it to our simulated haloes. The central and bottom panels of Fig. 10 show the distribution of the bias after applying the correction considering the scatter in the 2–10 keV band surface brightness and in the y -parameter, respectively. We report in Table 2 the values of the median of the corrected and uncorrected bias distributions together with their dispersion also for the other two X-ray bands, for our sample of 30 relaxed haloes. In all cases the systematics for relaxed systems is completely eliminated, with the halo to halo scatter which is reduced as well. A very small number of highly perturbed haloes keep having overestimates of 10–20 per cent: this reflects the presence of other types of asymmetries in the profiles not directly associated to the clumpiness of the ICM. Nevertheless, when calculating the median and the quartiles of the whole sample distribution, as shown in Table 3, we can see that our method is still effective even if applied “blindly” to all objects.

In Fig. 11 we show the radial dependence of $b(M_{\text{gas}})$ and of the corresponding bias after applying the X-ray and SZ corrections. Even close to the core, the uncorrected bias is significant (~ 5 per cent) and it grows linearly up to 10 (20) per cent at R_{200} for relaxed (perturbed) systems. We observe that already at distances corresponding to R_{500} ($\approx 0.7R_{200}$) the expected overestimate is already close to the values at R_{200} , with differences of the order of 2 per cent. When applying the corrections, we can clearly see that for relaxed objects the systematics is completely removed with value a of 0 ± 2 per cent up to $2R_{200}$. Even for perturbed haloes the improvement is consistent (a factor of ~ 3) through the whole radial range.

5.3 Correcting the hydrostatic-equilibrium mass bias

A frequently used method to determine the total mass of a galaxy cluster relies on the assumption that the ICM is in hydrostatic equilibrium. The measured density and temperature profiles are then used to determine the total mass $M_{\text{he}}(< r)$ enclosed by a given radial distance r

$$M_{\text{he}}(< r) = -\frac{k_{\text{B}}T(r)r}{G\mu m_{\text{p}}}\left(\frac{d\log \rho(r)}{d\log r} + \frac{d\log T(r)}{d\log r}\right), \quad (13)$$

where $T(r)$ is the (mass-weighted) temperature profile, and μ is the mean molecular weight in units of the proton mass, m_{p} . This method is known to be affected by several systematics associated to the break of the spherical symmetry and to the presence non-thermal pressure sources that affect particularly cluster outskirts (see Section 1). Here, instead, we focus on determining the bias associated to the residual clumpiness of the ICM.

It is easy to show that when accounting for the gas density bias of eq. (7), the X-ray measured hydrostatic-equilibrium mass $M_{\text{he,X}}$ formula contains an additional term associated to $C_{\mathcal{R}}$, thus becoming

$$\begin{aligned}M_{\text{he,X}}(< r) &= -\frac{k_{\text{B}}T(r)r}{G\mu m_{\text{p}}}\left(\frac{d\log \rho(r)}{d\log r} + \frac{d\log T(r)}{d\log r} + \right. \\ &\quad \left. + \frac{1}{2}\frac{d\log C_{\mathcal{R}}(r)}{d\log r}\right).\end{aligned}\quad (14)$$

Since $C_{\mathcal{R}}(r)$ generally grows with r (see Figs. 4 and 5), unlike $\rho(r)$ and $T(r)$, this turns into an underestimate of the value of M_{he} . To study this effect in detail, for every object of our sample we compute the true value of M_{he} and $M_{\text{he,X}}$ by adopting the following procedure. We first fit $T(r)$ in the range 0.8 – $1.2 R_{200}$, with the formula of Vikhlinin et al. (2006)⁵. Then, in the same radial range, we fit $\rho(r)$ and the biased density $\rho_{\text{X}}(r)$ profiles with a β -model

⁵ Here we consider only the external part of their profile, i. e. the formula of their eq. (4), after fixing $a = 1$ and $b = 2$, thus leaving only three free parameters: normalisation, core radius and the external slope c . However, since our objective is to determine the bias associated to the uncertainties in the density profile, any possible effect introduced by changing the temperature fitting procedure is negligible.

Table 2. Best-fit values of the parameters σ_0 and r_0 (second and third column, respectively, with r_0 in units of R_{200}) of the relation $C_{\rho}^{\text{est}}(\sigma, r)$, being σ the azimuthal scatter of the surface brightness in the three X-ray bands (second to fourth row) and the scatter of the y -parameter profiles (fifth row). The fourth column shows the median (in percent units) of the distributions of bias in the value of M_{gas} at R_{200} for our sample of 30 relaxed haloes, together with the difference with respect to the upper and lower quartiles (indicated as error), after the clumpiness correction of eq. (12). The fifth and sixth column show the same quantities for the distribution of M_{he} and f_{gas} , respectively. In the last row we report the values corresponding to the uncorrected biases.

	σ_0	r_0	$b(M_{\text{gas}}) \%$	$b(M_{\text{he}}) \%$	$b(f_{\text{gas}}) \%$
$\sigma_{\text{SB}} (0.3\text{--}0.8 \text{ keV})$	22.85	5.51	$+0.02^{+1.27}_{-0.85}$	$-0.56^{+1.68}_{-1.19}$	$+0.26^{+2.34}_{-1.31}$
$\sigma_{\text{SB}} (0.5\text{--}2 \text{ keV})$	16.02	5.87	$+0.08^{+1.22}_{-0.94}$	$-0.38^{+1.69}_{-1.19}$	$+0.06^{+2.38}_{-0.98}$
$\sigma_{\text{SB}} (2\text{--}10 \text{ keV})$	7.65	7.08	$-0.58^{+1.53}_{-0.67}$	$+0.55^{+1.87}_{-2.63}$	$-0.45^{+2.59}_{-1.34}$
σ_y	2.83	8.25	$-0.34^{+1.40}_{-0.89}$	$+0.95^{+1.84}_{-1.47}$	$-1.59^{+3.02}_{-1.27}$
No correction			$+6.11^{+1.73}_{-1.51}$	$-2.22^{+1.52}_{-2.02}$	$+8.45^{+2.57}_{-2.11}$

Table 3. Same as Table 2 but for the whole sample of 62 haloes. The best-fit σ_0 and r_0 are not quoted here since we assume the same values of the relaxed sample.

	$b(M_{\text{gas}}) \%$	$b(M_{\text{he}}) \%$	$b(f_{\text{gas}}) \%$
$\sigma_{\text{SB}} (0.3\text{--}0.8 \text{ keV})$	$+1.45^{+3.33}_{-1.54}$	$-0.35^{+2.53}_{-2.58}$	$+2.32^{+4.24}_{-2.86}$
$\sigma_{\text{SB}} (0.5\text{--}2 \text{ keV})$	$+1.42^{+2.99}_{-1.58}$	$-0.61^{+2.60}_{-2.56}$	$+2.18^{+3.85}_{-2.83}$
$\sigma_{\text{SB}} (2\text{--}10 \text{ keV})$	$+0.69^{+2.76}_{-1.36}$	$+0.64^{+2.80}_{-3.16}$	$+0.84^{+3.56}_{-3.16}$
σ_y	$+0.82^{+2.72}_{-1.38}$	$+1.23^{+3.17}_{-2.57}$	$-0.05^{+4.80}_{-3.90}$
No correction	$+8.26^{+4.03}_{-2.54}$	$-2.23^{+2.25}_{-3.59}$	$11.15^{+6.16}_{-3.17}$

(Cavaliere & Fusco-Femiano 1978) and use these results to compute M_{he} and $M_{\text{he,X}}$, respectively, with eq. (13) for $r = R_{200}$.

The top panel of Fig. 12 shows the distribution of the expected value of $b(M_{\text{he}})$ for our sample of simulated clusters and groups. While it is confirmed that for the majority of the cases (45 over 62) the residual clumpiness introduces an underestimate, since the clumping factor of single objects can be affected by local variations (i.e. $C_{\mathcal{R}}(r)$ is not perfectly monotonic), we end up with about a quarter of our sample in which the measured M_{he} is higher than the true value. As a general remark, the median effect of about -2 per cent is small when compared to the other systematics, and with respect to the intrinsic dispersion (~ 6 per cent difference between the upper and lower quartile). We note, however, that for the most disturbed systems the error can reach 10 per cent or more in either direction.

We repeat the same procedure done for $b(M_{\text{gas}})$ (see Section 5.2) to see whether our clumpiness-correction method is effective in reducing the value of $b(M_{\text{he}})$. The results for the three X-ray bands and for the SZ effect are shown in Table 2 and 3 and in the central and bottom panel of Fig. 12 for the hard 2–10 keV band and for the SZ effect only, respectively. Also in this case we observe a global improvement of the measurements, with the systematics that disappear in all cases. On the other side, the halo to halo scatter is not significantly reduced.

5.4 Correcting the gas fraction bias

The two biases associated to the residual clumpiness previously described (positive bias for M_{gas} and negative for M_{he}) add together

when measuring the gas fraction f_{gas} . In fact, being the measured value

$$f_{\text{gas,X}} = \frac{M_{\text{gas,X}}}{M_{\text{he,X}}}, \quad (15)$$

the corresponding bias is

$$b(f_{\text{gas}}) \equiv \frac{f_{\text{gas,X}} - f_{\text{gas}}}{f_{\text{gas}}} = \frac{b(M_{\text{gas}}) - b(M_{\text{he}})}{1 + b(M_{\text{he}})}. \quad (16)$$

When computing the value of $b(f_{\text{gas}})$ at $r = R_{200}$ for our sample of 62 haloes, we can see from the distribution shown in the top panel of Fig. 13 that this results in a systematic overestimate on average of about 10 per cent. The ICM inhomogeneities cause also a large spread in the measured value, with 11 objects having $b(f_{\text{gas}}) > 0.2$ (three are outside the plot range).

We verify the efficiency of our bias-correction method for f_{gas} by computing the expected value of $b(f_{\text{gas}})$ once the corrected values of $b(M_{\text{gas}})$ and $b(M_{\text{he}})$ (see Section 5.2 and 5.3, respectively) are used in eq. (16). We show the results in Table 2 and 3 and in the central and bottom panel of Fig. 13 (2–10 keV band and SZ effect only, respectively). Again, in all cases the average bias is significantly reduced, with σ_{SB} for the 2–10 keV band and σ_y that provide the best results. In this case, as for $b(M_{\text{he}})$, the application of our method allows also to reduce the scatter in the measured values.

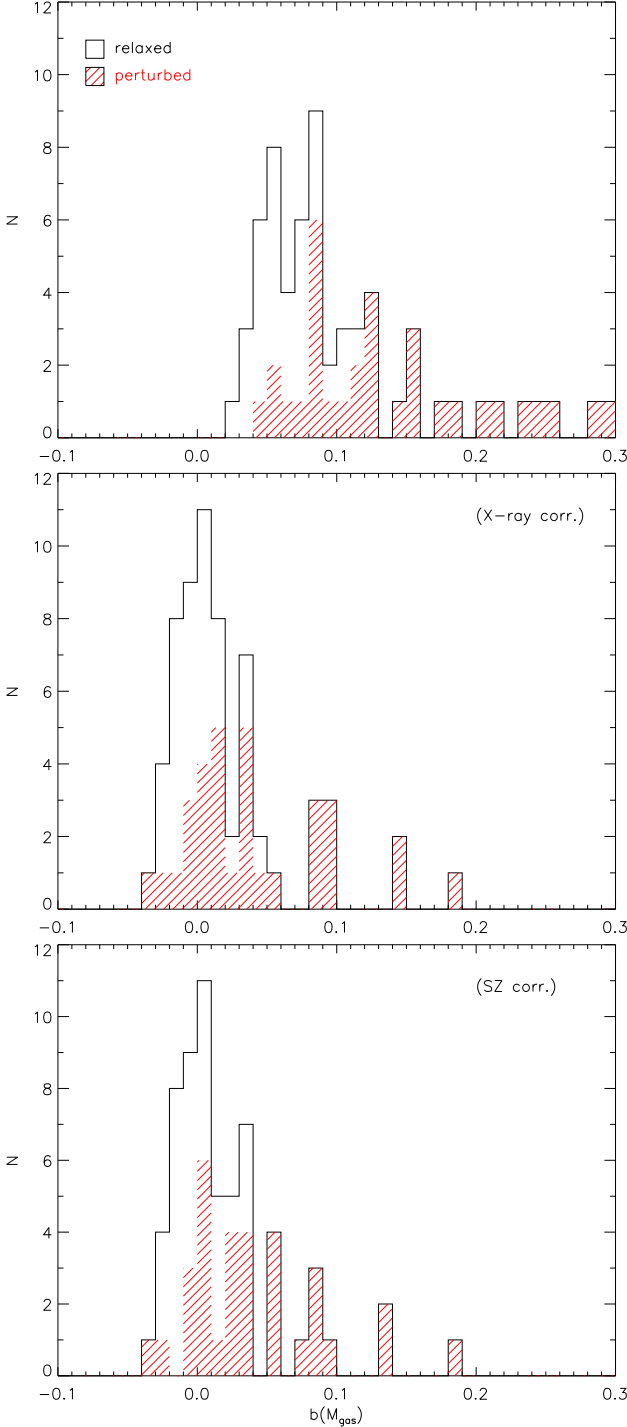


Figure 10. Top panel: histogram of the estimated gas mass bias associated to the residual clumpiness for our sample of 62 clusters. Perturbed haloes are marked by the shaded areas. Central and bottom panels: same as top panel but after the correction obtained by estimating the value of $C_{\mathcal{R}}$ from the scatter in the 2–10 keV surface brightness and y -parameter, respectively.

6 SUMMARY AND CONCLUSIONS

In this paper we have analyzed a set of 62 simulated clusters and groups, obtained with different physical prescriptions, with the objective of providing a global characterization of their density inhomogeneities in the regions close to the virial radius. We have described a method that allows to separate the ICM clumpiness as-

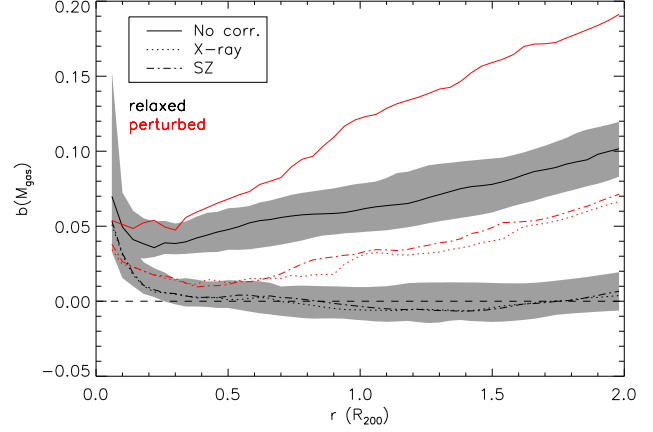


Figure 11. Bias in the value of M_{gas} as a function of distance from the centre for our reference physical model without correction (solid lines) and with the correction obtained by estimating the value of $C_{\mathcal{R}}$ from the scatter in the 2–10 keV surface brightness and y -parameter (dotted and dot-dashed lines, respectively). The black lines represent the median of the 30 relaxed objects and the grey-shaded regions enclose the quartiles of the uncorrected and of the X-ray corrected biases (the quartile region of the SZ corrected bias has a similar size). The red lines represent the median value for the perturbed sample. The horizontal dashed line corresponds to the value of $b(M_{\text{gas}})=0$.

sociated to small clumps from a “residual” one that corresponds to large-scale inhomogeneities, and discussed how the latter depends on the mass and the dynamical state of the halo. Finally, we have discussed how the presence of large-scale inhomogeneities can bias the estimates of M_{gas} , M_{he} and f_{gas} and provided a method to reduce this bias by using a directly observable quantity: the azimuthal scatter in the X-ray surface brightness profiles or in the thermal SZ ones (y -parameter profiles).

Our results can be summarized as follows.

- (i) As expected, the degree of global clumpiness in our simulated objects depends mainly on the presence/absence of radiative cooling, making about one order of magnitude difference. Once cooling is included, additional feedback mechanisms do not change significantly the clumping factor.
- (ii) When considering only the contribution of emitting gas, we obtain values of $C \simeq 2 - 3$ at R_{200} . When compared to the value of ~ 16 claimed by Simionescu et al. (2011), we conclude that their estimate can not be reproduced by our models, even neglecting the possibility of identifying emitting clumpy structures.
- (iii) We introduce the concept of *residual clumpiness*, $C_{\mathcal{R}}$, to quantify the amount of large-scale inhomogeneities (departure from spherical symmetry, presence of filaments), that corresponds to the bulk clumpiness once obvious bright condensed clumps are masked out. This quantity is independent of the physical model assumed, while it is sensitive to the dynamical state of the halo: relaxed objects have $C_{\mathcal{R}} \sim 1.2$ at R_{200} , while dynamically perturbed ones have on average $C_{\mathcal{R}} \sim 1.5$.
- (iv) The residual clumpiness of the ICM causes a significant overestimate in the measurement of M_{gas} from X-ray observations of the order of $\sim 5 - 10$ per cent for the more relaxed objects up to $\sim 20 - 30$ per cent for the more perturbed ones.
- (v) A smaller negative bias of about 2 per cent is present also in the measurement of M_{he} . Consequently, the combination of the two biases results in an overestimate of f_{gas} , with average values

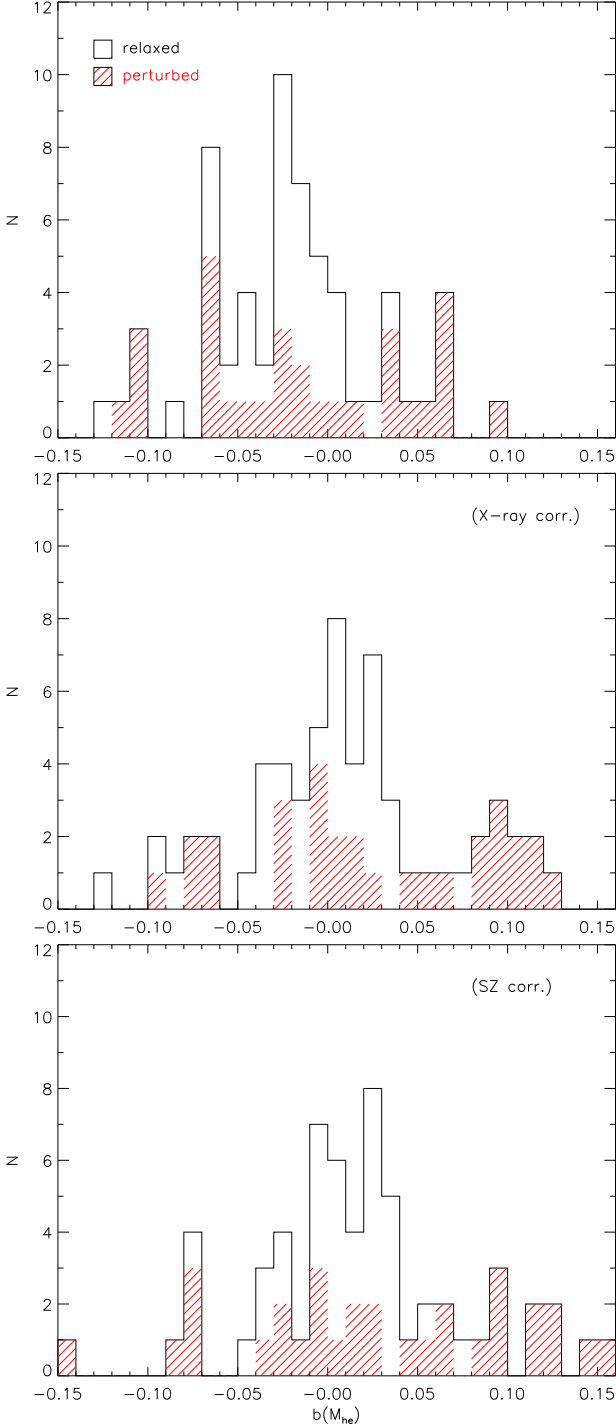


Figure 12. Same as Fig. 10 but for the bias in the hydrostatic-equilibrium mass. One perturbed haloes, D03-*a*, is not shown since its values are outside the plot range being, from top to bottom, $b(M_{\text{he}}) = -0.22, -0.21$ and -0.19 , respectively. D27-*a* is also outside the plot range in the top and central panels with $b(M_{\text{he}}) = -0.25$ and -0.17 , respectively.

of ~ 10 per cent, and an intrinsic scatter of ~ 9 per cent (interquartile range). These biases are lower when compared to other known systematics.

(vi) The residual clumpiness correlates well ($r_S = 0.6 - 0.7$) with the azimuthal scatter of the X-ray surface brightness and of the y -parameter profiles. This allows us to obtain an analytical formula to

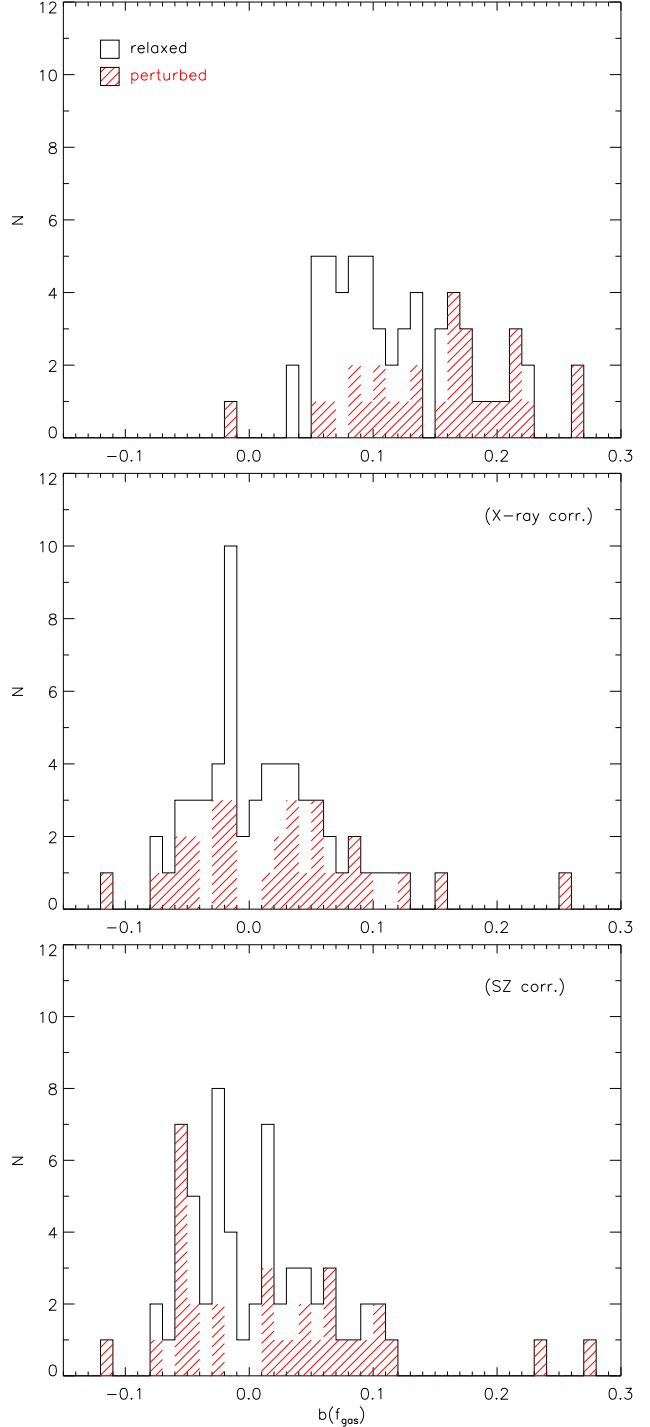


Figure 13. Same as Fig. 10 but for the bias in the gas fraction. Three perturbed haloes, D03-*a*, D18-*a* and D27-*a*, are not shown in the top panel since their values are outside the plot range: $b(f_{\text{gas}}) = 0.35, 0.33$ and 0.65 , respectively. D27-*a* is outside the plot range also in the central panel, having $b(f_{\text{gas}}) = 0.30$.

estimate it as a function of two observable variables: the azimuthal scatter and the radial distance.

(vii) This relation provides a method to correct the gas density estimates, making it possible to improve consistently the accuracy of the M_{gas} measurements. With this method the systematics described above disappears completely for relaxed haloes from out-

side the cluster core up $2R_{200}$. For perturbed clusters/groups the overestimate is reduced by a factor of about 3.

(viii) Finally, this method works also in eliminating the bias associated to the measurement of M_{he} and f_{gas} . However a large intrinsic scatter (5–7 per cent, in terms of interquartile range) between the different objects remains.

Overall, our results show how the study of the outskirts of galaxy clusters and groups is important for the measurement of the gas mass and gas fraction, and how the combination of simulations and observations can improve their precision. A possible extension and improvement of this analysis may be investigating the correlation of $C_{\mathcal{R}}$ with other inhomogeneities parameters such as the halo ellipticity, or by determining how the $C_{\mathcal{R}}(\sigma, r)$ relations may vary as a function of the observed relaxation parameters of the haloes.

ACKNOWLEDGMENTS

Most of the computations necessary for this work have been performed at the Italian SuperComputing Resource Allocation (ISCRA) of the Consorzio Interuniversitario del Nord Est per il Calcolo Automatico (CINECA). We acknowledge financial contributions from contracts ASI-INAF I/023/05/0, ASI-INAF I/088/06/0, ASI I/016/07/0 COFIS, ASI Euclid-DUNE I/064/08/0, ASIUni Bologna-Astronomy Dept. Euclid-NIS I/039/10/0, ASI-INAF I/023/12/0, the European Commissions FP7 Marie Curie Initial Training Network CosmoComp (PITN-GA-2009-238356), by the PRIN-MIUR09 “*Tracing the growth of structures in the Universe*” and by PRIN MIUR 2010-2011 “*The dark Universe and the cosmic evolution of baryons: from current surveys to Euclid*”. DF acknowledges funding from the Centre of Excellence for Space Sciences and Technologies SPACE-SI, an operation partly financed by the European Union, European Regional Development Fund and Republic of Slovenia, Ministry of Education, Science, Culture and Sport. We thank an anonymous referee that provided useful indications to improve the quality of our work. We acknowledge useful discussions with N. Cappelluti, G. Murante, E. Rasia and L. Tornatore. We are grateful to D. Eckert for providing us the data on the scatter of his observed profiles.

REFERENCES

- Allen S. W., Evrard A. E., Mantz A. B., 2011, *ARA&A*, 49, 409
- Andrade-Santos F., Lima Neto G. B., Laganá T. F., 2012, *ApJ*, 746, 139
- Basu K., et al., 2010, *A&A*, 519, A29
- Battaglia N., Bond J. R., Pfrommer C., Sievers J. L., 2012, *ApJ*, 758, 74
- Bautz M. W., Miller E. D., Sanders J. S., Arnaud K. A., Mushotzky R. F., Porter F. S., Hayashida K., Henry J. P., Hughes J. P., Kawaharada M., Makashima K., Sato M., Tamura T., 2009, *PASJ*, 61, 1117
- Birkinshaw M., 1999, *Phys. Rep.*, 310, 97
- Böhringer H., Pratt G. W., Arnaud M., Borgani S., Croston J. H., Ponman T. J., Ameglio S., Temple R. F., Dolag K., 2010, *A&A*, 514, A32
- Bonafede A., Dolag K., Stasyszyn F., Murante G., Borgani S., 2011, *MNRAS*, 418, 2234
- Buote D. A., Tsai J. C., 1995, *ApJ*, 452, 522
- Burns J. O., Skillman S. W., O’Shea B. W., 2010, *ApJ*, 721, 1105
- Cappelluti N., Ranalli P., Roncarelli M., Arevalo P., Zamorani G., Comastri A., Gilli R., Rovilos E., Vignali C., Allevato V., Finoguenov A., Miyaji T., Nicastro F., Georgantopoulos I., Kashlinsky A., 2012, *MNRAS*, 427, 651
- Cassano R., Ettori S., Giacintucci S., Brunetti G., Markevitch M., Venturi T., Gitti M., 2010, *ApJ*, 721, L82
- Cavaliere A., Fusco-Femiano R., 1978, *A&A*, 70, 677
- Churazov E., Vikhlinin A., Zhuravleva I., Schekochihin A., Parrish I., Sunyaev R., Forman W., Böhringer H., Randall S., 2012, *MNRAS*, 421, 1123
- De Filippis E., Sereno M., Bautz M. W., Longo G., 2005, *ApJ*, 625, 108
- Eckert D., Ettori S., Molendi S., Vazza F., Paltani S., 2013, *A&A*, 551, A23
- Eckert D., Vazza F., Ettori S., Molendi S., Nagai D., Lau E. T., Roncarelli M., Rossetti M., Snowden S. L., Gastaldello F., 2012, *A&A*, 541, A57
- Elvis M., et al., 2009, *ApJS*, 184, 158
- Fabjan D., Borgani S., Tornatore L., Saro A., Murante G., Dolag K., 2010, *MNRAS*, 401, 1670
- Ferland G. J., Korista K. T., Verner D. A., Ferguson J. W., Kingdon J. B., Verner E. M., 1998, *PASP*, 110, 761
- George M. R., Fabian A. C., Sanders J. S., Young A. J., Russell H. R., 2009, *MNRAS*, 395, 657
- Haardt F., Madau P., 1996, *ApJ*, 461, 20
- Hoshino A., Henry J. P., Sato K., Akamatsu H., Yokota W., Sasaki S., Ishisaki Y., Ohashi T., Bautz M., Fukazawa Y., Kawano N., Furuzawa A., Hayashida K., Tawa N., Hughes J. P., Kokubun M., Tamura T., 2010, *PASJ*, 62, 371
- Humphrey P. J., Buote D. A., Brighenti F., Flohic H. M. L. G., Gastaldello F., Mathews W. G., 2012, *ApJ*, 748, 11
- Iapichino L., Niemeyer J. C., 2008, *MNRAS*, 388, 1089
- Jeltema T. E., Canizares C. R., Bautz M. W., Buote D. A., 2005, *ApJ*, 624, 606
- Kawahara H., Reese E. D., Kitayama T., Sasaki S., Suto Y., 2008, *ApJ*, 687, 936
- Kawaharada M., Okabe N., Umetsu K., Takizawa M., Matsushita K., Fukazawa Y., Hamana T., Miyazaki S., Nakazawa K., Ohashi T., 2010, *ApJ*, 714, 423
- Khedekar S., Churazov E., Kravtsov A., Zhuravleva I., Lau E. T., Nagai D., Sunyaev R., 2012, *ArXiv e-prints*
- Kravtsov A. V., Borgani S., 2012, *ARA&A*, 50, 353
- Mitchell N. L., McCarthy I. G., Bower R. G., Theuns T., Crain R. A., 2009, *MNRAS*, 395, 180
- Morandi A., Limousin M., Sayers J., Golwala S. R., Czakon N. G., Pierpaoli E., Jullo E., Richard J., Ameglio S., 2012, *MNRAS*, 425, 2069
- Nagai D., Lau E. T., 2011, *ApJ*, 731, L10
- Nelson K., Rudd D. H., Shaw L., Nagai D., 2012, *ApJ*, 751, 121
- Piffaretti R., Valdarnini R., 2008, *A&A*, 491, 71
- Planck Collaboration 2012, *ArXiv e-prints*
- Planelles S., Borgani S., Dolag K., Ettori S., Fabjan D., Murante G., Tornatore L., 2012, p. 44
- Rasia E., Ettori S., Moscardini L., Mazzotta P., Borgani S., Dolag K., Tormen G., Cheng L. M., Diaferio A., 2006, *MNRAS*, 369, 2013
- Rasia E., Meneghetti M., Martino R., Borgani S., Bonafede A., Dolag K., Ettori S., Fabjan D., Giocoli C., Mazzotta P., Merten J., Radovich M., Tornatore L., 2012, *New Journal of Physics*, 14, 055018
- Rephaeli Y., Sadeh S., Shimon M., 2005, in Melchiorri F., Rephaeli Y., eds, *Background Microwave Radiation and Intra-*

- cluster Cosmology The Sunyaev-Zeldovich effect. pp 57–+
- Roncarelli M., Cappelluti N., Borgani S., Branchini E., Moscardini L., 2012, MNRAS, 424, 1012
- Roncarelli M., Moscardini L., Borgani S., Dolag K., 2007, MNRAS, 378, 1259
- Roncarelli M., Moscardini L., Tozzi P., Borgani S., Cheng L. M., Diaferio A., Dolag K., Murante G., 2006a, MNRAS, 368, 74
- Roncarelli M., Ettori S., Dolag K., Moscardini L., Borgani S., Murante G., 2006b, MNRAS, 373, 1339
- Sanders J. S., Fabian A. C., 2012, MNRAS, 421, 726
- Sato T., et al., 2012, PASJ, 64, 95
- Sayers J., Czapon N. G., Mantz A., Golwala S. R., Ameglio S., Downes T. P., Koch P. M., Lin K.-Y., Maughan B. J., Molnar S. M., Moustakas L., Mroczkowski T., Pierpaoli E., Shitanishi J. A., Siegel S., Umetsu K., Van der Pyl N., 2012, ArXiv e-prints
- Schuecker P., Finoguenov A., Miniati F., Böhringer H., Briel U. G., 2004, A&A, 426, 387
- Sereno M., Ettori S., Baldi A., 2012, MNRAS, 419, 2646
- Sijacki D., Springel V., Di Matteo T., Hernquist L., 2007, MNRAS, 380, 877
- Sijacki D., Vogelsberger M., Kereš D., Springel V., Hernquist L., 2012, MNRAS, 424, 2999
- Simionescu A., Allen S. W., Mantz A., Werner N., Takei Y., Morris R. G., Fabian A. C., Sanders J. S., Nulsen P. E. J., George M. R., Taylor G. B., 2011, Science, 331, 1576
- Simionescu A., Werner N., Urban O., Allen S. W., Fabian A. C., Sanders J. S., Mantz A., Nulsen P. E. J., Takei Y., 2012, ApJ, 757, 182
- Smith R. K., Brickhouse N. S., Liedahl D. A., Raymond J. C., 2001, ApJ, 556, L91
- Springel V., 2005, MNRAS, 364, 1105
- Springel V., Hernquist L., 2003, MNRAS, 339, 289
- Sunyaev R. A., Zeldovich Y. B., 1970, Ap&SS, 7, 3
- Tormen G., Bouchet F. R., White S. D. M., 1997, MNRAS, 286, 865
- Tornatore L., Borgani S., Dolag K., Matteucci F., 2007, MNRAS, 382, 1050
- Vazza F., Brunetti G., Kritsuk A., Wagner R., Gheller C., Norman M., 2009, A&A, 504, 33
- Vazza F., Eckert D., Simionescu A., Brueggen M., Ettori S., 2012, ArXiv e-prints
- Vazza F., Roncarelli M., Ettori S., Dolag K., 2011, MNRAS, 413, 2305
- Vikhlinin A., Kravtsov A., Forman W., Jones C., Markevitch M., Murray S. S., Van Speybroeck L., 2006, ApJ, 640, 691
- Walker S. A., Fabian A. C., Sanders J. S., George M. R., 2012, MNRAS, 427, L45
- Wiersma R. P. C., Schaye J., Smith B. D., 2009, MNRAS, 393, 99
- Zhuravleva I., Churazov E., Kravtsov A., Lau E. T., Nagai D., Sunyaev R., 2013, MNRAS, 428, 3274

APPENDIX A: IDENTIFYING CLUMPS WITH OBSERVATIONS

Our volume-clipping method, described in Section 3.2 and more in detail in Roncarelli et al. (2006b), allows us to separate between the gas belonging to clumps and to the bulk of the cluster based on theoretical considerations. Here we provide more information on the physical properties of these clumps and investigate up to which extent they may be detected in simulated X-ray surface brightness

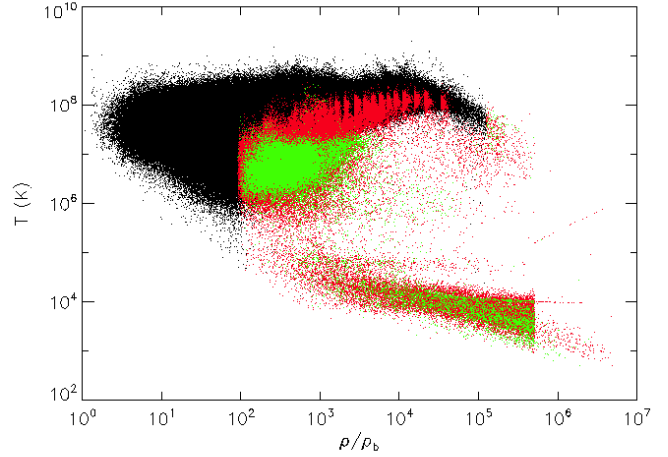


Figure A1. Phase diagram of the SPH particles outside $0.5R_{200}$ of the D17-a simulated cluster for our reference model. The black points indicate the particles of the bulk. The particles identified as clumps by our algorithm are marked in green if they fall inside a contour region of the right panel of Fig. A2, and red otherwise.

maps, and whether the different methods would introduce significant biases in the C_R determination.

We show in Fig. A1 the $T - \rho$ scatter plot of the SPH particles in the outskirts of the D17-a relaxed cluster. The amount of gas that our algorithm associates to the clumpy phase (red and green points) corresponds to about the 3 per cent of the total gas mass inside R_{200} for this halo. We verified that in perturbed systems it is slightly higher (4–5 per cent). By analysing the plot, the multi-phase nature of these clumps shows up clearly. Part of the gas is associated to the cold star-forming phase at $\rho > 10^3 \rho_b$ and $T = 10^4 - 10^5$ K. These particles are responsible for most of the global ICM clumpiness (see the comments on Fig. 4) but would not influence any X-ray measurement since their temperature is too low to produce any significant emission. The majority of clump particles, which usually embed the previous ones, are instead at higher temperature ($T > 10^6$ K) and can eventually produce a detectable X-ray emission.

The maps of Fig. A2 show the 0.5–2 keV surface brightness, up to $2R_{200}$ of the bulk (left panel) and of the clumps (right) of the D17-a relaxed cluster, as defined by our method. The great homogeneity of the bulk map shows clearly that no clumpy structure is missed by our filtering method and that any possible detectable inhomogeneity must necessarily be associated to the clump phase. The possibility of detecting them depends on how much their signal is brighter with respect to the bulk one. To this purpose we identified the map regions where the signal-to-noise ratio exceeds a value of 3, by considering the bulk map as a reference for the noise. Most of the clumpy structures are at least partially identified with this method, with an increasing efficiency towards the outskirts.

In Fig. A3 we show the surface brightness of the identified clumps as a function of distance from the centre, compared to the average cluster surface brightness profile. Since the central part of these clumps is usually very bright, in most of the cases their average surface brightness exceeds the cluster one by more than 5. It is clear also, that these structures can be identified also outside R_{200} , since their signal is well above the unresolved X-ray background, at least in the case of a massive halo.

As a drawback of our method, when in a given radial bin no clear clumpy structure is present we consider as clumps also a small

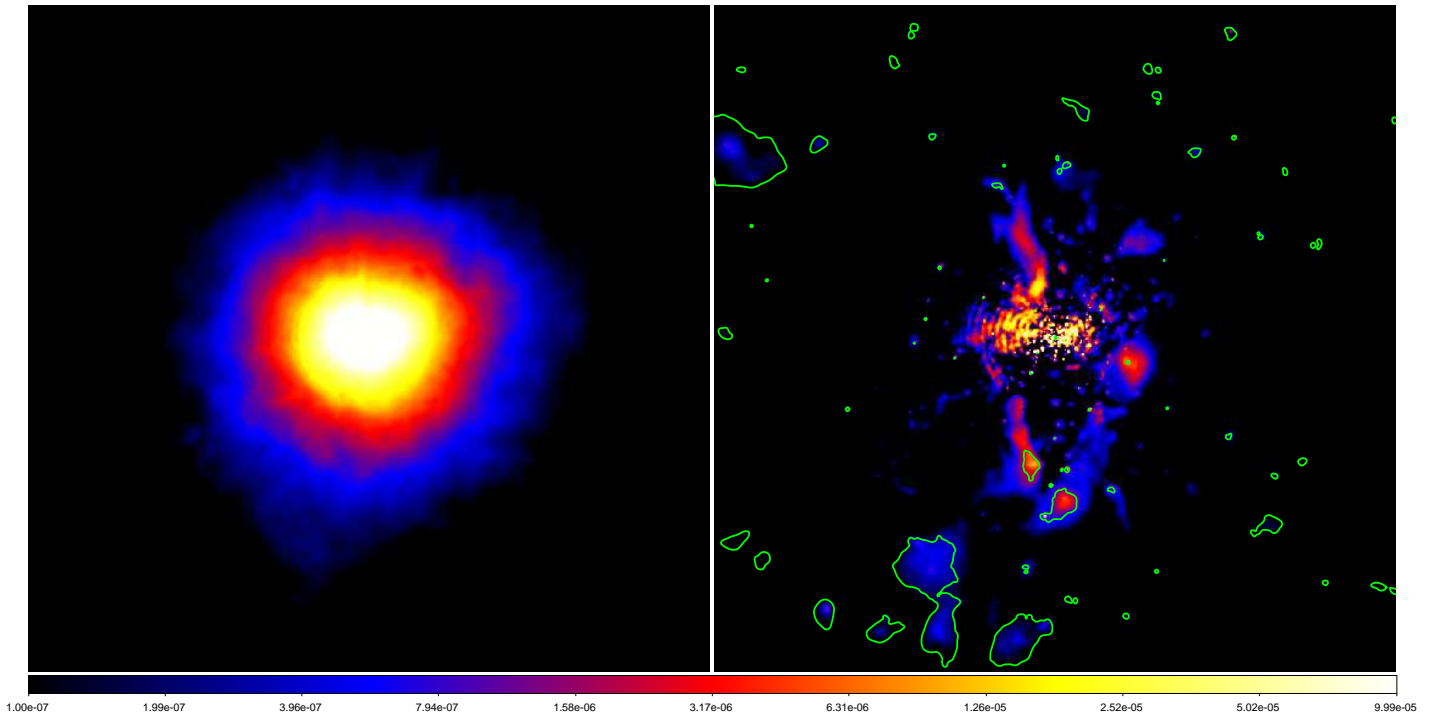


Figure A2. Maps of the soft (0.5–2 keV) X-ray surface brightness of the D17-a cluster for our reference model in units of $\text{counts s}^{-1} \text{cm}^{-2} \text{arcmin}^{-2}$. Each map is centered on the cluster centre and encloses a square of $4R_{200}$ per side. Left panel: the gas which is identified as ‘bulk’ by our theoretical filtering method (99 per cent volume). Right panel: the gas which is identified as ‘clumps’ (one per cent volume). The contours enclose the regions where the projected clumps signal is more than 3 times the bulk one, mimicking a $S/N > 3$ threshold.

fraction of diffuse gas whose signal is not high enough to be identified. This happens in particular in the regions close to the centre where the ICM is more uniform, as it can be seen both in the right panel of Fig. A2 and by the red points of Fig. A2. A precise determination of the fraction of clumps that would be missed by real X-ray observations clearly depends on instrumental details and is beyond the aim of our work which focuses on the large-scale inhomogeneities. However, using our mock maps we can provide an estimate of the amount of missed clumpy gas, together with its influence on the bias of the gas mass measurements. We verified that the detected clumpy ICM (e.g. green particles in Fig. A2) is the ~ 20 per cent of the total amount of gas associated to clumps by our volume-clipping method. In order to have an estimate of its impact on the mass gas measurement, we repeated our analysis by reducing by a factor of 5 the volume threshold (i.e. the 0.2 per cent of the volume of each bin). We obtained a value of $b(M_{\text{gas}}) = 7.7$ per cent for the relaxed sample, with respect to the previous 6.1 (see Table 2) obtained with our more conservative threshold. Therefore, given the relatively small difference, we conclude that the impact on our results of any unresolved clumpy gas is minor with respect to the one associated to large-scale inhomogeneities.

APPENDIX B: RELAXED AND PERTURBED HALOES FROM AN OBSERVATIONAL POINT OF VIEW

In Section 3.2 we have described our classification of simulated haloes into *relaxed* and *perturbed* according to the robustness of the determination of $C_{\mathcal{R}}$. Here we explain how this criterium, which is

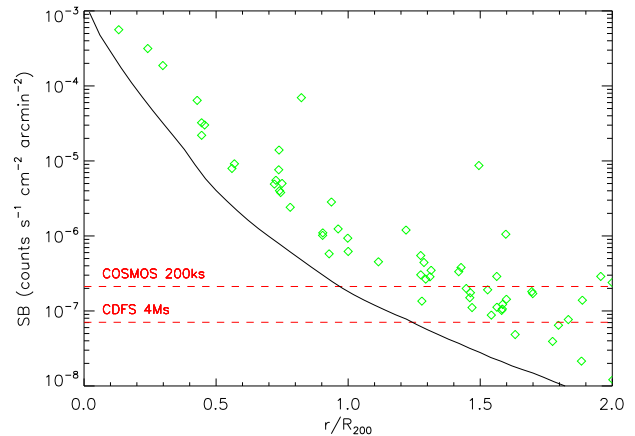


Figure A3. Soft (0.5–2 keV) X-ray surface brightness of the clumps (green diamonds) identified with the method shown in Fig. A2 as a function of distance from the centre. The black solid line represents the average surface brightness of the cluster bulk. The red dashed lines indicate the measurements of the unresolved X-ray background in the same band from the COSMOS survey (Elvis et al. 2009, ~ 200 ks exposure, upper line) and from the 4Ms Chandra Deep Field South (Cappelluti et al. 2012, lower line).

based on purely theoretical considerations, actually matches well with a possible classification done with observational methods.

To this purpose we have created a 0.5–2 keV band surface brightness map for each of our simulated objects. Following Cassano et al. (2010), we have then computed, over the radial

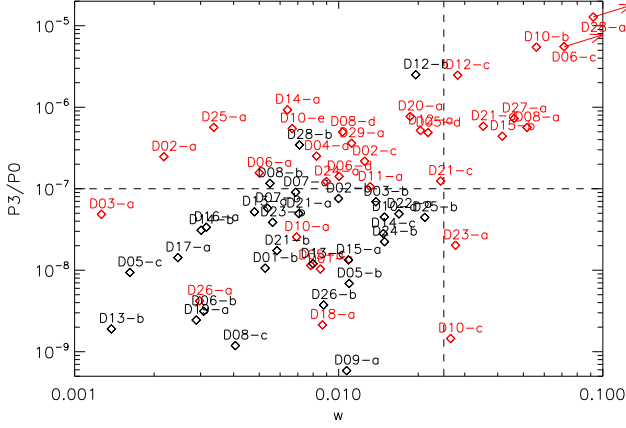


Figure B1. Power-ratio P_3/P_0 versus the centroid shift w estimated from the 0.5–2 keV surface brightness maps in the radial range $0.1-1 R_{200}$ for the sample of our 62 simulated clusters and groups. The two objects indicated with arrows have values outside the plot range. The two dashed lines indicate the limits of $w = 0.025$ and $P_3/P_0 = 10^{-7}$ that provide the best match between the two definitions of relaxed/perturbed halos (see text).

range $0.1 - 1R_{200}$, the centroid shift w , defined as the standard deviation, in units of R_{200} , of the projected separation between the X-ray peak and the centroid, and the power-ratio P_3/P_0 (see Buote & Tsai 1995), that is the lowest normalized moment of the X-ray surface brightness clearly connected to substructures (see, e.g., Böhringer et al. 2010). We show in Fig. B1 the position of our simulated systems in the P_3/P_0 vs w plane. Haloes defined as relaxed according to our definition (marked in black) have on average lower values of all the parameters, thus sitting on the lower left corner of the plot, while perturbed ones tend to show a high value in at least one of the two parameters.

The dashed lines ($w = 0.025$ and $P_3/P_0 = 10^{-7}$) show the limits that roughly correspond to the best match between the two classifications. When defining observationally the relaxed haloes as the ones laying on the bottom-left quadrant of the plot, and perturbed otherwise, we end up with 53 over 62 haloes matching the corresponding theoretical definition.